Mouse sensorimotor cortex reflects complex kinematic details during reaching and grasping

Authors: Harrison A. Grier[1], Sohrab Salimian[1], Matthew T. Kaufman[2,3,4*]

Affiliations:
[1] Graduate Program in Computational Neuroscience, The University of Chicago, Chicago, IL 60637
[2] Dept. of Organismal Biology and Anatomy, The University of Chicago, Chicago, IL 60637
[3] Neuroscience Institute, The University of Chicago, Chicago, IL 60637
[4] NSF-Simons National Institute for Theory and Mathematics in Biology

[*] indicates corresponding author

Funding:
This work was funded by The University of Chicago, NSF-NCS 1835390, NIH-NINDS R01 NS121535, the Simons Foundation, the Sloan Foundation, the Whitehall Foundation, and the NSF-Simons National Institute for Theory and Mathematics in Biology via grants NSF DMS-2235451 and Simons Foundation MP-TMPS-00005320.

Author contributions:
H.G., Experimental design, Data acquisition, Keypoint frame labeling, Analysis and interpretation of data, Drafting and revising the manuscript; S.S. Keypoint frame labeling, Analysis and interpretation of data; M.K, Project conception, Supervision of all aspects of the project, Experimental design, Data preprocessing, Drafting and revising the manuscript, Funding.

Acknowledgements:
We thank M. Rivers and R. Vescovi for assistance with installing and configuring the high-speed camera platform, D. Sabatini for help setting up the behaviors and discussions of analysis, P. Ravishankar for animal care assistance, S. Musall for widefield imaging code, and the Maunsell, MacLean, Sheffield, and Giovannucci Labs for aid with reagents, transgenics, image debugging, and calcium data preprocessing.

Data availability:
Data are available on figshare. Code used to create the figures is available on GitHub: https://github.com/kaufmanlab/waterGrab-public.

Abstract

Coordinated forelimb actions, such as reaching and grasping, rely on motor commands that span a spectrum from abstract target specification to detailed instantaneous muscle control. The sensorimotor cortex is central to controlling these complex movements, yet how the detailed command signals are distributed across its numerous subregions remains unclear. In particular, in mice it is unknown if the primary motor (M1) and somatosensory (S1) cortices represent low-level joint angle details in addition to high-level signals like movement direction. Here, we combine high quality markerless tracking and two-photon imaging during a reach-to-grasp task to quantify movement-related activity in the mouse caudal forelimb area (CFA) and forelimb S1 (fS1). Linear decoding models reveal a strong representation of proximal and distal joint angles in both areas, and both areas support joint angle decoding with comparable fidelity. Despite shared low-level encoding, the time course of high-level target-specific information varied across areas. CFA exhibited early onset and sustained encoding of target-specific signals while fS1 was more transiently modulated around lift onset. These results reveal both shared and unique contributions of CFA and fS1 to reaching and grasping, implicating a more distributed cortical circuit for mouse forelimb control than has been previously considered.

Introduction

Primary motor cortex (M1) and primary somatosensory cortex (S1) are the neocortical structures most strongly and directly connected to the sensorimotor periphery. Accordingly, signals related to movement are strongly present in M1 (Evarts 1973; Galiñanes et al. 2018; Georgopoulos et al. 1982; Moran and Schwartz 1999; Park et al. 2022; Saleh et al. 2012; Sauerbrei et al. 2020), and signals related to both cutaneous and proprioceptive somatosensation are strongly present in S1 (Alonso et al. 2023; Chowdhury et al. 2020; Costanzo and Gardner 1981; Fromm and Evarts 1982; Gardner and Costanzo 1981; Pei et al. 2009; Prsa et al. 2019; Umeda et al. 2019). Yet despite being among the longest-studied brain structures, our understanding of these areas' exact roles in movement production remains incomplete (Omrani et al. 2017).

M1 and S1 are strongly interconnected (Yamawaki et al. 2021) and work closely together (Nelson 1996): sensory signals are often strongly present in M1 (Lucier et al. 1975; Lemon et al. 1976; Evarts and Fromm 1977; Wong et al. 1978; Fetz et al. 1980; Fromm et al. 1984; Alonso et al. 2023; Asanuma 1975), and movement related signals are often present in S1 (Chowdhury et al. 2020; Cohen et al. 1994; Goodman et al. 2019; Nelson 1987; O'Connor et al. 2021; Prud'homme and Kalaska 1994; Tanji and Wise 1981; Umeda et al. 2019; Weber et al. 2011). Nevertheless, stimulation in M1 produces movement much more readily than in S1 (Penfield and Boldrey 1937), and lesions (Lawrence and Kuypers 1968; Whishaw et al. 1993; Kawai et al. 2015; Mizes et al. 2023, 2024; Nicholas and Yttri 2024) and inactivations (Galiñanes et al. 2018; Guo et al. 2015; Morandell and Huber 2017; Miri et al. 2017; Hwang et al. 2019; Sauerbrei et al. 2020; Hwang et al. 2021; Park et al. 2022) of M1 produce strong deficits in movement production, especially for movements that are kinematically complex (Bollu et al. 2024), flexible (Heindorf et al. 2018; Mizes et al. 2023), or coordinated across the hand and arm (Guo et al. 2015).

In monkeys, motor cortical activity has been argued to relate to high-level signals, such as movement endpoint (Georgopoulos et al. 1986) or hand velocity (Ashe and Georgopoulos 1994; Kalaska et al. 1983; Wang et al. 2007); or, low-level signals such as joint kinematics (Vargas-Irwin et al. 2010; Saleh et al. 2012, 2010; Goodman et al. 2019; Omlor et al. 2019; Okorokova et al. 2020) or muscle forces (Kakei et al. 1999; Lemon et al. 1986; Miri et al. 2017; Morrow and Miller 2003; Warriner et al. 2022); or even very detailed control previously thought to be reserved for the spinal cord, such as selecting types of motor pools (Marshall et al. 2022). The presence of signals at all of these levels suggests that monkey M1 may play a role in multiple levels of control. However, it is challenging to tease these roles apart in a model system where fine-grained causal perturbations and circuit tools are less developed.

The mouse has emerged recently as a model of interest for dissecting motor control (Warriner et al. 2020). As a model system, it offers high throughput, detailed atlases through both anatomical and functional tracing (BRAIN Initiative Cell Census Network (BICCN) et al. 2021; Muñoz-Castañeda et al. 2021; Winnubst et al. 2019; Zingg et al. 2014), and powerful techniques for large-scale recording (Manley et al. 2024; Steinmetz et al. 2021; Yu et al. 2021) and perturbation (Guo et al. 2015, 2021; Sauerbrei et al. 2020). However, the study of systems-level motor control in actively behaving animals is less mature in the mouse than in primates.

Extensive motor mapping experiments in rodents have revealed that activating different parts of the sensorimotor cortex evokes movements of different body parts or different kinds of movements of the same body part, as it does in primates (for review, see (Harrison and Murphy 2014)). Yet it is unclear how the topography of stimulation-evoked movements relates to the roles of these areas during volitional actions. Behavioral tasks in mice involving forelimb lever or reaching movements have provided a coarse-level understanding of how these areas contribute during behavior. Inactivations and lesions of M1 and S1 have shown that M1 is required for the execution of dexterous reach-to-grasp movements (Guo et al. 2015; Sauerbrei et al. 2020) and that S1 is essential for adapting learned movements to external perturbations of a joystick (Mathis et al. 2017). However, stimulation of brainstem nuclei alone can also evoke naturalistic forelimb actions, including realistic reaching movements involving coordinated flexion and extension of the proximal and distal limb (Esposito et al. 2014; Ruder et al. 2021; Yang et al. 2023). A key question is therefore what role M1 and S1 play in forelimb movement control. Namely, are these areas dominated by coarse, high-level signals while brainstem structures control the movement details? Or, is mouse sensorimotor cortex involved in controlling fine-grained movement features as in the monkey?

Here we characterize what kinematic information is present in M1 and S1 as a first step towards answering this question. To do so we combine a reach-to-grasp-to-drink paradigm (based on (Galiñanes et al. 2018; Galinanes and Huber 2023)) with detailed high-speed behavior tracking and two-photon calcium imaging to ask what movement-related signals are present in mouse M1 and S1. Decoding models revealed that both M1 and S1 encode fine details of movement in the mouse, enabling decoding of all 24 joint angles we reconstructed from the shoulder to digits – even features such as digit splay and opposition within the paw. Differences between the areas emerged only in the decoding of higher-level aspects of the task: M1 reflected target location earlier than S1 and S1 reflected movement initiation time more accurately than M1. Our results link M1 and S1 activity to the execution of reach-to-grasp movements and highlight their distinct yet complementary roles in encoding low-level kinematic details and higher-order movement features.

Results

Complex movement kinematics during mouse reaching and grasping movements

Assessing the relationship between neural activity and the details of movement requires striking a balance between achieving repeatable behavior and evoking sufficient trial-to-trial variability to avoid model overfitting. To achieve this balance, we modified a previously-developed water-reaching task (Galiñanes et al. 2018) to evoke challenging reaching and grasping movements to two locations (Fig. 1A). Importantly, the task setup was made compatible with high-speed stereo camera imaging and modern markerless tracking techniques for tracking putative joint centers, allowing for a detailed quantification of reaching trajectories and grasp attempts. Using a custom 3D-aware frame-labeling GUI and large numbers of labeled frames, we achieved high-quality tracking on nearly every frame (99% of lift-locked frames passed quality assurance for all 24 joint angles; 94.5% of trials were tracked usably; see Methods). This allowed us to quantify the kinematics at a fine level of detail and to obtain a more comprehensive description of these movements through joint angle kinematics (see Fig. 3).

Our task involved two water spout targets fixed in place on either side of the mouse's head at distances near the extent of the mouse's reach. After an initial hold period, the animals were instructed to reach to a specific spout by the pitch of a cue tone, which occurred simultaneously with water delivery at that spout. The probability of each spout being cued was 50% on each trial, so the animal had no information as to where they should reach until the cue was played. After the cue, they performed rapid reaching and grasping movements to retrieve the water reward from the spout (Fig. 1B). The mice produced reach trajectories with substantial variability around the basic reach shapes (Fig. 1C), likely resulting from small differences in initial posture causing execution errors and corrections. Three design choices increased this movement complexity: (1) the water spouts were located near the maximal range of motion of each animal, (2) the water spouts were designed so that water would cling to them, and (3) we required good contact between the paw and the spout using touch sensors. As a result, the mice often displayed repeated grasp attempts to contact the spout and retrieve the entire water droplet (Fig 1G). This variability across trials, spout targets, and mice was also seen in trial events like lift reaction time, reach duration, time-to-first-contact, and the number of contact events that occurred within 1 second of the cue on each trial (Fig. 1D-G).

In similar tasks, optogenetic inactivation of mouse M1 can halt the ongoing execution of reaching and grasping movements (Galiñanes et al. 2018; Guo et al. 2015). However, given that many of our mice performed the task for upward of 8 weeks and evidence that motor cortex disengages after extensive practice with lever pressing (Hwang et al. 2019, 2021; Kawai et al. 2015), it was not clear whether motor cortex would remain necessary in our task. To determine this, we performed optogenetic inactivations of the Caudal Forelimb Area (CFA) in M1 (Muñoz-Castañeda et al. 2021; Tennant et al. 2011) by activating inhibitory neurons in two VGAT-ChR2 mice. These inactivations blocked the execution of the reach to grasp sequence, preventing the animal from making contact with the spout during the 3-second laser stimulation period (Fig. 1F; 86.5% control trials with contact within 3 seconds of cue, 5.1% inactivation trials with contact, $P < 10^{-191}$, Mann-Whitney U test, 2 mice, 495 stimulation trials). Interestingly, inactivation at the time of cue often did not prevent reach initiation (mouse 1: 54.7%, mouse 2:

34.2% of inactivation trials with lift within 3 seconds; 93.5%, 86.2% control trials). Yet the movement stalled once the paw and digits extended towards the spout, producing uncoordinated and unsuccessful reaching trajectories (Fig. 1I, two representative datasets).

Stereotyped aperture kinematics across idiosyncratic reach-to-grasp movements

Rodent forelimb movements have been described qualitatively as a set of sequential stereotyped postures when reaching to grasp food or water rewards (Whishaw and Pellis 1990) (Fig. 1B). We identified these features in our data using our high precision quantification of the mouse's proximal and distal forelimb during reaching. First, we defined a simple geometric measure of paw aperture that captured the strongest features of paw opening and closing, including the splay of the digits and flexion of the metacarpophalangeal (MCP) and proximal interphalangeal joints (PIP) (Fig. 2A). The first aperture minimum corresponded tightly with the peak of vertical paw velocity after lifting, with the paw reaching maximum vertical velocity shortly before the paw and digits became maximally flexed (Fig. 2B) (r=0.6-0.95 across mice, Pearson correlation; maximum velocity preceded minimum aperture by 27.2 ± 10.5 ms across mice). When aligning single-trial aperture traces to the peak vertical velocity (max Z velocity), we observed clear, stereotyped structure in how paw aperture evolved during the movements, across both spout targets for all five mice (Fig. 2E). This stereotyped shape was surprising given the heterogeneity in reach trajectories in this task and the strong differences in reaching strategies adopted for each target.

We termed the first aperture minimum after the lift to be the time of "collect," following (Whishaw et al. 2010), and termed the next maximum after collect "extend" (Fig. 2B). These events structured the elaboration of the reach-to-grasp movement over time: after lifting, the paw closed to its minimum aperture (collect) before the digits were maximally opened (extend) as the paw was moved towards the spout. Extend occurred more heterogeneously in time after collect (Fig. 2C), perhaps reflecting single-trial variability in initial posture. These grasp-related events corresponded strongly with the reach's progress as well. Regardless of the initial paw location on the paw rest, lifting the arm brought the flexing paw to a consistent location at the moment of collect, from which the mouse could prepare an accurate extension movement towards the spout (Fig. 2D). These observations serve as quantitative confirmation of previous qualitative details obtained from high speed video and confirm rich structure in the mouse reach-to-grasp movement.

Proximal and distal joints are coordinated during mouse reach-to-grasp

To obtain a high fidelity representation of the reach-to-grasp kinematics, we constructed a 3D "skeletal" representation of the forelimb by video-tracking keypoints at 15 putative joint centers along the proximal and distal axis (Methods). We then used axis-angle geometries to approximate 24 joint angles (7 proximal, 17 distal), including a number of intrapaw angles that captured deformations of the paw itself (Fig. 3A). These joint angles displayed rich temporal heterogeneity when reaching and grasping to both targets (Fig. 3B). Joint angles were strongly correlated across the entire limb, consistent with the expectation that the forelimb is a system of joints that are controlled cooperatively and, in some cases, are mechanically linked (Fig. 3C). The strongest correlations occurred for angles describing the same joint (e.g., the 3 angles describing the shoulder) and for the flexion of MCP and PIP joints. The block-like structure of

the joint angle correlation matrices indicated that control of the mouse distal limb is tightly linked to control of the proximal limb, consistent with previous observations of the strong stereotypy in mouse forelimb movements across behaviors (Naghizadeh et al. 2020; Whishaw 1996; Whishaw et al. 2010; Whishaw and Pellis 1990).

Despite the strong coupling between the proximal and distal joint angles, rich variation remained in the action of different joints over time. To assess the number of linearly independent degrees of freedom amongst the 24 joint angles and velocities, we used double-cross-validated PCA (Yu et al. 2009); Methods; Fig. 3D), finding intermediate dimensionalities of 7 (median for joint angles) and 10 (velocities; Fig. 3E). This is consistent with the idea that joint angles across the limb are coordinated instead of controlled independently, and that this coordination is flexible enough over time to enable accurately performing reaching and grasping to different targets.

Layer 2/3 cells in CFA and fS1 are strongly modulated and heterogeneously tuned

Having characterized the structure of the mouse forelimb reaching and grasping movements, we next sought to determine how the kinematic details of these movements were distributed across the sensorimotor cortex. To do so, we recorded neural activity from neurons in layer 2/3 of the caudal forelimb area of M1 (CFA) extending into the immediately adjacent secondary motor cortex (M2), and the forelimb region of S1 (fS1) using two-photon calcium imaging. A slight majority of recorded neurons in both areas (51.8% in CFA and 52.2% in fS1, $p < 0.05$ with Bonferroni correction at n=6) were statistically modulated to at least one event during the task: cue, paw lift, and/or first spout contact (Fig. 4B; see Methods, “ZETA”). Cells showed strong modulation locked to different task events, such as the cue onset (51.7% / 52.7% in CFA / fS1, left or right p-value < 0.05 corrected at n=2), paw lifting from the rest (51.6% / 54.8% in CFA / fS1), and time of first contact with the spout (45.2% / 46.4% in CFA / fS1). 7

Cells were also modulated by the time taken to complete the reach: many cells exhibited different firing rates on trials with movement duration briefer versus longer than the median (Fig. 4C-D, see ROIs 35 and 116). Finally, many cells showed temporal heterogeneity in their activity beyond that of simple transient bumps. This included cells (such as ROI 54) that were strongly modulated by movement onset and remained active late into the trial. This activity may reflect the details of movement as the animals made repeated grasping attempts with a fully extended arm to retrieve the entire water reward from the spout.

Proximal and distal joint kinematics can be decoded from CFA and fS1 population activity

To assess how movement related signals were distributed across CFA and fS1, we decoded the time series of each joint angle from neural population activity in each area. A simple linear regression model related the single-trial joint angles at all time points to single-trial neural activity at the corresponding moments. We found that every measured proximal and distal joint angle could be decoded from CFA activity at above-chance levels during reaching and grasping (Fig. 5A-B). Interestingly, fS1 decoding exhibited similar decoding performance as CFA across all mice (Fig. 5E-F).

Across both areas we found that proximal joints were better decoded than distal joints (Fig. 5D,H). A number of reasons for this difference are possible: this may reflect the time scale of 2p-recorded neural activity, overall smaller total variance of the most distal joint angles (see

Fig. 5S2E-F), or measurement noise present in the markerless tracking for small features like the fingertips. Nevertheless, we were able to explain substantial variance in the most distal intrapaw joints (see joints MCPf, MCPa, MCPo, PIPs and PIPf).

Additionally, we reconstructed the skeletal representation of the forelimb from the decoded joint angles and found that the reconstructed postures generally closely tracked the true trajectories, even of “minor” angles like cylindrical paw deformation or digit splay (Fig. 5C,G). This suggests that movement-related signals that could be used to actuate forelimb joints are present in both CFA and fS1 populations.

Finally, we tested whether the ability to decode these many joint angles was a direct consequence of inter-joint correlations, and might not be indicative of the presence of “real” information about some of these joints. To do so, we fit partial correlation models that removed correlations between proximal and distal joints, or removed correlations of the joint angles with a high-level parameter, the overall distance of the paw centroid to the spout. Despite substantially lowering the behavioral variance, the residuals could still be decoded from neural activity (Fig 5S2A-D). Overall, these results suggest that instantaneous movement-related signals are similarly distributed across CFA and fS1.

CFA reflects target-specific information earlier and more persistently than fS1

To assess whether higher-level target-related signals were present in each area, we analyzed how well target identity could be decoded from neural activity over time. For each session, a linear decoder was trained to predict whether the neural activity from a particular window of time came from a left-target or right-target trial. This decoder was then applied to held-out trials from the same time window. This analysis revealed that CFA activity reflected the target location slightly more faithfully than did fS1, as shown by its higher overall performance (93.2% CFA vs. 89.1% fS1 median over cross-validation folds and time bins; $p = 4.1 \times 10^{-4}$, Wilcoxon rank sum test). To examine single trials, we then projected each trial’s population activity onto the identified decoding axis (the “target-specific dimension”). In this projection, CFA activity predicted the target sooner after the cue than did fS1 activity (59.9 ± 34.7 ms earlier) and displayed a stronger, more consistent, and longer-lasting prediction throughout the trial (Fig. 6A,B).

To determine whether the target-specific dimension was conserved or whether it changed over the course of a movement, we then tested how well a decoder trained during one time window generalized to data from other time windows. CFA decoders were more stable over the trial, and performed better when generalizing to far-away time points than did fS1 decoders (Fig. 6C). These results suggest that the encoding of target-specific information is more consistent over time in CFA than fS1.

Finally, we asked how strongly each area encoded a different high-level parameter, resting versus reaching. To do so, we trained a decoder to predict whether neural activity was from a time point pre- or post-lift, then computed a movement onset time from when the decoder switched from pre- to post- (Methods; Fig. 6D). Unlike our results for predicting target identity, fS1 activity more strongly predicted lift time than did CFA.

Discussion

The extent to which activity in sensorimotor cortex reflects the details of movement has remained unclear in the mouse. Here we show that in a challenging reach-to-grasp task evoking variable movements, both CFA and fS1 relate tightly to all the joint angles we could track throughout the arm, paw and digits. Using high-fidelity markerless tracking, we replicated prior, coarser results that the reach-to-grasp kinematics have stereotyped structure and involve strong coordination across proximal and distal joints. Using two-photon calcium imaging, we revealed that single neuron activity in CFA and fS1 is strongly modulated and tuned to fine movement features. Decoding models then demonstrated that CFA and fS1 both possess rich representations of low-level joint angle information at similar levels of fidelity. Despite these similarities, target decoders revealed that movement information emerges more quickly at the population level after the cue and persists longer in CFA than it does in fS1. Activity in fS1 is thus more transient and more closely linked to lift onset than in CFA.

The strength of movement-related activity in these areas is surprising given the results of loss-of-function experiments in rodents, which have suggested that sensorimotor cortex can become disengaged from forelimb control with extensive training (Hwang et al. 2019, 2021; Kawai et al. 2015), and that subcortical structures like the medulla or basal ganglia can independently control coordinated forelimb movements (Esposito et al. 2014; Ruder et al. 2021; Yang et al. 2023). Our finding of low-level kinematic information in sensorimotor cortex suggests a role for cortex beyond simply providing high-level commands to these subcortical areas.

There are a number of possible roles for this movement-related cortical activity. One is that motor cortex may dominate control when the behavior is complex enough in some way – like when a cue is needed to identify the target (Mizes et al. 2024) or when sensory feedback is necessary to coordinate dexterous grasps in the presence of errors (Guo et al. 2015; Perich et al. 2024; Sauerbrei et al. 2020). Despite the overtraining of our behavior, these task features might preclude use of the presumably less-flexible subcortical circuits alone. Alternatively, subcortical areas like the medulla or cerebellum may initiate the movement (Dacre et al. 2021; Esposito et al. 2014; Inagaki et al. 2022; Ruder et al. 2021) while the cortex elaborates the details of otherwise-generic commands (Kaufman et al. 2016). This might permit the previously-observed disengagement of cortex with learning of simple behaviors, could explain our observations of partially executed reach-to-grasp movements during CFA inactivation, and would explain the weak representation of lift-onset in our CFA data. A third alternative is that medulla alone executes low-level control, but low-level information is maintained in sensorimotor cortex for some other function, such as to enable learning (Kawai et al. 2015; Makino et al. 2016; Wolff et al. 2022). These hypotheses are not mutually exclusive.

Our observation of detailed kinematic signals in the mouse forelimb somatosensory cortex raises the possibility of a central role for fS1 in dexterous movements, and may implicate a more broadly distributed circuit in forelimb control than previously considered. Indeed, the magnitudes of representation in CFA and fS1 were nearly identical. This may simply be a consequence of widely distributed representations of movement across mouse cortex (Musall et al. 2019; Steinmetz et al. 2019; Stringer et al. 2019), including forelimb somatosensory areas. However, the strength of detailed kinematic information in fS1 suggests a role beyond simply receiving a broad corollary discharge signal.

One possibility is that proprioceptive signals are strong enough to carry these movement details into fS1 from subcortical structures, as is true in primate forelimb S1 (Umeda et al. 2019). Our lift time decoding results are consistent with this view and align with recent observations characterizing mouse proprioceptive forelimb cortex spanning both S1 and M1 (Alonso et al. 2023). Further, our task evoked repetitive grasping attempts, which may engage fS1 strongly to inform motor areas of the sensory consequences of movement (Perich et al. 2024). Extensive circuit tracing has shown that forelimb M1 and forelimb S1 are highly interconnected in the mouse (Muñoz-Castañeda et al. 2021; Yamawaki et al. 2021), suggesting that detailed movement signals in fS1 may reflect not only sensory feedback but also efference copies of motor commands generated by CFA. Rodent fS1 is known to influence interneuron populations in the spinal cord through direct and indirect projections (Ueno et al. 2018), and thus these signals may also reflect fS1's important role in modulating reflex circuits in cooperation with movement generation (Moreno-López et al. 2016; Moreno-Lopez et al. 2021; Seki et al. 2003).

Several limitations of the present work should be noted. Pose estimation was performed with state-of-the-art neural networks (Mathis et al. 2018) and extensive hand-labeling of keypoints together with quality assurance metrics, but behavior tracking is inevitably imperfect. In particular, a noise floor remains that particularly impacts small bones such as the distal phalanges, and markers estimated at the skin surface cannot perfectly reflect underlying joint and muscle kinematics. Additionally, calcium imaging has limited temporal resolution and is a nonlinear transformation of spiking activity (Stringer and Pachitariu 2019; Wei et al. 2020). Although we used leading-edge deconvolution methods (Friedrich et al. 2017) and cutting-edge neural network approaches for sub-frame event estimation (Zhu et al. 2022), these limitations cannot be entirely overcome. These slow temporal dynamics limited our ability to disambiguate whether joint angles or joint velocities are more linearly encoded in these areas. Nevertheless, our ability to decode substantial variance from small joint angles and fast changes within the paw supports the claim that movement signals are represented in CFA and fS1 activity. Finally, all recordings included here were taken from layer 2/3 of both CFA and fS1. Activity may differ in layer 5, where the primary subcortical outputs originate.

Overall our results suggest that mouse sensorimotor cortex is intimately involved in the control of dexterous forelimb movements, and support use of the mouse as a first-class model system for studying the cellular and circuit basis of motor control. Further work will be required to map the roles of other sensorimotor cortical areas, understand their interactions, and differentiate between ballistic reaching and feedback-driven grasping and withdrawal.

Methods

Animal subjects

All procedures were approved by the University of Chicago Institutional Animal Care and Use Committee. A portion of the data presented here were analyzed in a previous study (mice 1 and 2; (Zhu et al. 2022)). For two-photon imaging, five male male Ai148D transgenic mice (TIT2L-GC6f-ICL-tTA2, stock 030328; Jackson Laboratory) aged 8-12 weeks were used. Four of the mice carried the GCaMP6f transgene heterozygously and one homozygously (mouse 3). For optogenetic experiments, 2 VGAT-ChR2 (stock 014548; Jackson Laboratory) transgenic mice aged 8-12 weeks were used. Each animal underwent a single surgery. Mice were then individually housed in a reverse 12-h light/dark cycle, with an ambient temperature of 71.5 °F and a humidity of 58%. Experiments were conducted in the afternoon, during the animal's dark cycle.

Surgical procedures

Mice were injected subcutaneously with dexamethasone (8 mg kg^{-1}) 24h and 1h before surgery to reduce inflammation. Mice were anesthetized with 2–3% inhaled isoflurane gas and then injected intraperitoneally with a ketamine–medetomidine solution (60 mg kg^{-1} ketamine and 0.25 mg kg^{-1} medetomidine). Mice were given supplemental low level isoflurane (0–1%) if they showed any signs that the depth of anesthesia was insufficient or began emerging from anesthesia towards the end of the surgery. Animals received a subcutaneous injection of meloxicam (2 mg kg^{-1}) at the beginning of the surgery and once daily for 2 days post-operation. The scalp was shaved, cleaned and resected, then the skull was cleaned and the wound margins glued to the skull with tissue glue (VetBond, 3M). A circular craniotomy was then made with a 3-mm or 4-mm biopsy punch centered over the left CFA / fS1 border. The coordinates for the center of CFA were taken to be 0.4 mm anterior and 1.5 mm lateral of bregma. The craniotomy was cleaned with SurgiFoam (Ethicon) soaked in phosphate-buffered solution (PBS). If the dura remained intact, a durotomy was performed.

Virus (AAV9-CaMKII-Cre, diluted to 1×10^{13} particles per mL in PBS, Addgene stock 105558-AAV9) was then pressure injected (NanoJect III, Drummond Scientific) at 2-6 sites near the target site, with 140 nL injected at each of two depths per site (250 and 500 μm below the pia) over 5 min each. The injection pipette was kept in place for another 3-6 minutes to ensure viral dispersion before being removed slowly over 2-3 minutes. In mice numbers 3-5 an additional virus injection (AAVretro-tdTomato, diluted to 1×10^{13} particles per mL in PBS, Addgene stock 59462-AAVrg) of 60-100 nL was made targeting the bulk of forelimb somatosensory cortex at -0.73 ± 0.08 mm posterior and ~2.69 ± 0.15 mm lateral of bregma. This injection retrogradely labeled cell bodies in CFA that sent projections to fS1. In this paper the labeling was used solely for stabilizing the imaging plane (see below) in both areas. In mice 1 and 2, a small craniotomy was made using a dental drill over the right CFA at 0.4 mm anterior and 1.6 mm lateral of bregma. 140 nL of AAVretro-tdTomato (1×10^{13} particles per mL, Addgene) was then injected at 300 μm below the pia. This injection labeled cells in the left CFA projecting to the contralateral CFA. As above, this labeling was used solely for stabilizing the imaging plane.

The injection craniotomy was sealed with a drop of Kwik-Cast (World Precision Instruments). For mice 1-3 and the two VGAT-ChR2 mice the cranial window craniotomy was sealed with a custom cylindrical glass plug (3 mm in diameter, 660 μm in depth; Tower Optical) bonded (Norland Optical Adhesive 61, Norland) to a 4-mm number 1 round coverslip (Harvard Apparatus) that was glued to the skull surface with tissue glue. For mice 4 and 5 the craniotomy was sealed with a custom metal and glass cannula created from a small stainless steel ring (3.96 mm outer diameter, 3.45 mm inner diameter, 0.76 mm length, MicroGroup) bonded to a 4 mm number 1 round coverslip using cyanoacrylate glue (ZAP-A-GAP, Robart). All window implants were glued in place first with tissue glue (VetBond) and then with cyanoacrylate glue (Krazy Glue) mixed with dental acrylic powder (Ortho Jet; Lang Dental). In all mice two layers of MetaBond (Parkell) were applied, and then a custom laser-cut titanium head bar was affixed to the skull with black dental acrylic. Animals were awoken by administering atipamezole via intraperitoneal injection and allowed to recover at least 3 days before water restriction.

Behavioral task

As previously reported (Zhu et al. 2022), the behavioral task (Fig. 1) was a variant of the water-reaching task of (Galiñanes et al. 2018) that we term the 'water grab' task. This task was performed by water-restricted, head-fixed mice, with the forepaws beginning on paw rests (eyelet screws) and the hindpaws and body supported by a custom, 3D-printed, tapered, clear acrylic tube enclosure. After holding the paw rests for 700–900 ms, a tone was played by stereo speakers and a 2- to 3-μl droplet of water appeared at one of two water spouts (22 gauge, 90-degree bent, 1-in blunt dispensing needles, McMaster) positioned on either side of the snout. The pitch of the tone indicated the location of the water, with a 4 kHz tone indicating left and a 7 kHz tone indicating right. The cue tone lasted 500 ms or until the mouse made contact with the correct water spout, whichever came first. The mouse could grab the water droplet and bring it to its mouth to drink any time after the tone began. Both the paw rests and spouts were wired with capacitive touch sensors (Teensy 3.2, PJRC). Good contact with the correct spout produced an intertrial interval of 3–6 s, while failure to make contact (or insufficiently strong contact) with the spout produced an intertrial interval of 20 s. Because the touch sensors required good contact from the paw, this setup encouraged complex contacts with the spouts. Control software was custom written in MATLAB R2018a using PsychToolbox 3.0.14. Touch event monitoring and task control were performed at 60 Hz using the Teensy.

Behavioral task training

The mice were trained to make all reaches with the right paw and to keep the left paw on the paw rest during reaching. For the first 1-3 days, mice were head-fixed and provided water directly to their mouths to acclimate them to head-fixation and reward collection. During this period the animals were encouraged to make consistent contact with both paw rests to trigger water delivery at their mouths. After acclimation and consistent trial initiation the spout was withdrawn to a position on the right side of their face intended to elicit forelimb reaching with the right arm. If animals were reluctant to reach, small droplets of water were placed on their right whisker pad with a blunt syringe to induce grooming and water collection. After animals reliably performed reaches toward the rightward spout location (>80-90% success), another spout was installed near the initial location (the "left" spout). Water was then solely delivered through the

left spout and its position was shifted across the midline to the ventral contralateral whisker pad over the course of 7-10 days. Once the left spout was in a nearly-equidistant location from the midline as the right spout, the animal was cued to reach to both spouts in blocks of 10-50 trials. After reaching >90% in blocked trials, trials were cued randomly. This training procedure took 2-4 weeks, although the behavior continued to solidify for at least two more weeks. Data presented here were collected after 6–8 weeks' experience with the task.

Optogenetic inhibition

Two VGAT-ChR2 mice were trained to perform the task. After 6-8 weeks of training, inactivations were performed using the epifluorescence path of our 2-photon microscope, centered over coordinates 1.5L 0.5A from bregma. The stimulation protocol was designed to approximately replicate the experiments of (Guo et al. 2015). Pulses were 17 mW peak power, 12.5 ms long and delivered at 40 Hz (50% duty cycle, 8.5 mW average power). The spot of light was approximately 1.3 mm in diameter at the focal plane. Stimulation was delivered beginning 150 ms before the cue and then pulsed continuously for 3 seconds after the cue. After an initial behavioral warm-up period of 50 control trials, stimulation was delivered with 25% probability on subsequent trials. To compensate for visible blue light due to leak around the light-sealing cone or through the brain, two bright blue LED strips were placed in front of the animal and illuminated constantly throughout the session.

High speed videography and stereo triangulation

As previously reported (Zhu et al. 2022), high-speed video data was recorded using a pair of cameras (BFS-U316S2M-CS, FLIR; varifocal lenses COZ2813CSIR2, Computar) mounted 150 mm from the right paw rest at 10° apart. Infrared illuminators enabled behavioral imaging while performing 2p imaging in a darkened microscope enclosure. Cameras were synchronized and recorded at 150 frames per second with real-time image cropping and JPEG compression and streamed to one HDF5 file per camera (areaDetector module of EPICS, CARS). DeepLabCut (DLC) (Mathis et al. 2018) was used to track 15 keypoints in each image (see next section). The MATLAB Stereo Camera Calibration toolbox was used for estimation of stereo camera parameters to triangulate paired keypoints into 3D.

Markerless tracking

3-5 days before recording, the right forelimb of each mouse was shaved and depilated using Nair while the animal was under light anesthesia (1-2% isoflurane). We did not observe any obvious impacts of this depilation on the behavior. DLC was then used to identify 15 keypoints associated with bony landmarks spanning the proximal and distal forelimb. These keypoints included: the tip (#1-4), proximal interphalangeal joints (#5-8) (PIP) and metacarpal phalangeal joints (#9-12) (MCP) of each digit, the center of the wrist (#13), distal edge of the elbow joint (#14), and proximal tip of the lesser tubercle of the humerus (#15). We developed a custom GUI in Python to improve the quality of manually labeled training frames. This GUI allowed simultaneous labeling in both images and visualized the epipolar lines of each keypoint in each image to improve stereo correspondence. We then employed an active learning approach to create a dataset of manually labeled images. First, 20-80 frames paired between cameras were randomly selected from all 12 datasets. These images were manually labeled for

all 15 markers and an initial DLC model was trained to identify keypoint locations for both cameras. We then performed 3 rounds of active learning, selecting 15-35 additional paired frames per dataset per round. We selected frames for inclusion in each round by identifying 3D postures in each video that strongly differed from those already contained in the training set (Feng et al. 2023). We assessed the similarity of candidate frames in a window 300-1000 ms around the water cue to the training set by computing the sum of Euclidean distances between vectorized 3D keypoint positions. We then sorted candidate frames by this distance and manually selected additional frames to label from the 10% of candidate frames with the greatest total distance. At the end of this process we labeled a total of 1455 paired images across 12 datasets (100-165 images per dataset) for a total of 2910 high quality labeled images.

Joint angle kinematics

To extract joint angle kinematics from the 3D triangulated keypoints, we first obtained vectors connecting adjacent keypoints in the unsmoothed data. Because we chose keypoint locations to closely align with putative joint centers across the forelimb, the angles between vectors connecting keypoints were taken to approximate the angles associated with the joint.

For the shoulder joint, we identified the “humerus” with the vector pointing from the shoulder keypoint to the elbow keypoint. For the elbow joint we identified the “radius/ulna” with the vector from elbow to wrist. The vector used to compute wrist angles pointed from wrist to the mean of the second and third MCP keypoints (virtual MC or vMC). For each digit, we computed the vector connecting the corresponding MCP to PIP keypoints, and finally the PIP to DIP keypoints. The vectors defined in this way were used to compute extrinsic Euler angles around each of the putative joint centers in a proximal-to-distal fashion. After each joint angle was computed, the corresponding vector and all of its children vectors were rotated so as to neutralize the rotation around that joint.

We chose a coordinate system appropriate for our task in mice. Starting with the shoulder joint, we computed the abduction/adduction of the humerus as the rotation around the external (world) Y axis (green vector in Fig. 3A) necessary to bring the humerus into the ZY plane; abduction was chosen to be negative and adduction was positive. Next we computed the flexion/extension as the rotation around the X axis (red vector in Fig. 3A) required to align the humerus with the Z axis (blue vector in Fig 3A); flexion was positive. Finally, we computed the shoulder rotation as the angle around the Z axis required to bring the radius/ulna into the YZ plane; internal rotation was positive. At the elbow we computed flexion/extension as the angle around the X axis required to make the radius/ulna parallel to the Y axis; flexion was positive. We followed a similar procedure for the wrist as the shoulder; abduction/adduction was computed as the angle around the X axis required to bring the vMC into the XY plane; radial deviation or adduction was positive. We computed the wrist flexion/extension as the angle around the Z axis that brought the vMC into the YZ plane; flexion was positive. Finally, to compute the wrist rotation we first obtained the vector normal to the plane spanned by the second and third MCP vectors (nMCP). Wrist “rotation” (torsion of the radius around the ulna) was computed as the angle around the Y axis required to bring the nMCP into the YZ plane; pronation was positive. We then computed two intermetacarpal angles, quantifying how “opposed” MCP1 or MCP4 was to MCP2 or MCP3 respectively. This measure quantifies the conical deformation of the paw. This was done by computing the angle around the Y axis

required to bring the MCP1 or MCP4 vectors into the YZ plane so that they were coplanar with MCP2 and MCP3. We calculated paw splay for the metacarpal 1-2, 2-3, and 3-4 vectors as the angle around the Z axis required to bring them into the XY plane. We then computed two angles around each MCP joint: abduction/adduction and flexion/extension. MCP abduction/adduction was computed as the angle around the X axis required to bring the proximal phalanx into the XY plane; abduction from the wrist midline was positive. We computed the metacarpal flexion/extension as the angle around the Z axis required to bring the proximal phalanx vector into the YZ plane; flexion was positive. Finally, we computed the PIP flexion as the angle between the distal phalanx and the proximal phalanx for each digit.

Trial screening

To identify trials with problematic keypoint tracking, we used the extracted joint angle kinematics. We first binned joint angles for each trial at 10 ms in a window from -100 ms to 400 ms locked to lift onset and smoothed with a 15 ms Gaussian kernel. Left and right trials were considered separately. For each joint angle we found the 2.5 and 97.5 percentile values (pctile1 and pctile2) across all trials and time points. We then computed threshold values for each joint angle as (pctile1 + pctile2) / 2 ± abs(pctile1 - pctile2). Across all trials, we identified individual joint angle values that exceeded the bounds of these two thresholds. Next, for each trial we computed the number of time bins for which any joint angle was outside the bounds. If a trial had more than 5 such time bins it was excluded from further analysis. Across all mice this procedure identified 4719/4993 trials with high quality tracking, which were further confirmed by visual inspection. After screening, no substantial tracking errors were detected even on single frames, and thus no further cleaning was performed.

Joint angle correlations and dimensionality

As in the screening procedure we first binned at 10 ms, locked joint angles from -100 ms to 400 ms relative to lift onset, and smoothed each angle within trials with a 15 ms Gaussian kernel. We then concatenated all trials across time. To exclude unusual joint angle configurations due to contact forces, we removed time points during which the paw made contact with the spout target. We then computed the correlation matrix shown in Figure 3 using the *corrcoef* MATLAB function on this concatenated matrix. To compute the dimensionality of the joint angles and joint velocities, we performed double cross-validated principal component analysis (PCA) on the same concatenated matrix (Yu et al. 2009). To perform this procedure, we first held out a subset of observations and performed PCA. Then, for each held-out observation, we held out one joint, used the values of the other joints together with the loadings to estimate the low-D coordinates on that observation via regression, and finally estimated the value of held-out joint in the held-out observations from the low-D coordinates and the loading for that joint. After cycling over all variables and 5 random observation partitions for each candidate dimensionality, we identified the optimal dimensionality as the one that minimized the reconstruction error of the held-out variable in the held-out observations. This procedure was performed separately for joint angles and joint velocities.

Wide-field imaging for area identification

To identify the forelimb primary somatosensory cortex, we performed widefield imaging while providing sensory input to the contralateral paw using a vibration motor (SparkFun, part ROB-08449) glued to a paw rest (Alonso et al. 2023). This provided vibrotactile stimulation of the entire forelimb. The mouse was in the type of behavioral setup they were accustomed to except for the paw rest, and did not have to perform any task. Vibration was delivered for 250 ms once the mouse's paws had been on the paw rests for at least 2 seconds.

The widefield macroscope was identical to the setup of (Musall et al. 2019), except that a pco.panda 4.2 sCMOS camera (Excelitas) was substituted and LED triggers were delivered by a Teensy 3.2. Imaging was performed at 30 frames/s, alternating blue and violet illumination. Violet frames were used for hemodynamic correction.

We used the locus of stimulation-evoked activity to align each cranial window to the Allen Common Coordinate Framework v3. The location of strongest activation was aligned with the center of the widest part of the CCF area named S1-fl (roughly 0 AP 2.6 ML relative to bregma), where proprioceptive and tactile responses most strongly overlap. We targeted our S1 imaging fields of view to this location and referred to the recorded region as forelimb S1 or fS1 as done in (Alonso et al. 2023). With the window aligned to the atlas, we identified CFA as a compromise between this alignment and the coordinates of 0.4 AP and 1.6 ML relative to bregma. We targeted our CFA imaging field of views to this region. In some cases, thick vasculature or weaker indicator expression prevented high-quality imaging of the ideal location. In these few cases, we imaged as close as possible to the target. Results were similar between all datasets.

Two-photon imaging

Calcium imaging procedures have been described previously. Briefly, imaging was performed with a Neurolabware 2p microscope running Scanbox 4.1 and a pulsed Ti:sapphire laser (Vision II, Coherent). Depth stability of the imaging plane was maintained using a custom plugin that made automatic movements of the objective up to every ~10s based on comparing acquired red-channel data with an initially-acquired image stack. Offline, images were run through Suite2p to perform motion correction, region-of-interest (ROI) detection and fluorescence extraction. ROIs were manually curated using the Suite2p GUI. As previously described (Zhu et al. 2022), fluorescence was neuropil-corrected, detrended, and passed through OASIS using the 'thresholded' method, AR1 event model, and limiting the tau parameter to be between 300 and 800 ms. Neurons were discarded if they did not meet a minimum SNR criterion. To put events on a more useful scaling, for each ROI, we found the distribution of event sizes, smoothed the distribution (ksdensity in MATLAB, with an Epanechnikov kernel and log transform), found the peak of the smoothed distribution and divided all event sizes by this value. This rescales the peak of the distribution to have a value of unity.

When time-locking the data for visualization, modulation testing, or for decoding analyses, the deconvolved events were resampled into 10-ms bins. This resampling was performed by assigning a fraction of each event into the new 10-ms bins proportionally to how much the 10-ms bins overlapped the original ~32.2 ms frames, and taking into account the exact time

each ROI centroid was sampled based on its position within the field of view (FOV). Alignment for RADICaL has been described previously (Zhu et al. 2022).

Modulation index

To test whether regions of interest (ROIs) were task responsive, we adapted the "ZETA" method from (Montijn et al. 2021) to time series data, closely related to the approach used in (Heimel et al. 2023). The goal of this procedure was to determine whether the activity of each ROI was reliably modulated over time relative to some task event, such as cue or paw lift. Left and right trials were considered separately, and Bonferroni correction for multiple comparisons was performed at the end. First, neural data for all trials were resampled to 10 ms as described in the previous section. For each ROI, we averaged activity over trials and computed its fractional cumulative sum over time bins. This cumulative sum was compared to the linear baseline that would be expected from an ROI that fired uniformly at a matched rate in the same time window. The deviation of the cumulative sum from the linear baseline (i.e., the residuals) was computed, then this deviation trace was mean centered and its maximum absolute value was found. This value was the data maximum deviation. We then generated a null distribution for this statistic. To do so, we shuffled by circularly permuting the event-locked data independently for each trial before averaging across trials, mean-centering, and computing the shuffle's maximum deviation as above. This procedure was repeated 100 times to produce the distribution for the maximum deviation under the null hypothesis that the cell fired uniformly over time. We then computed the p-value as the probability of observing the data maximum deviation under a Gumbel distribution parameterized by the mean and variance of the distribution of maximum deviations over shuffles. Compared to the ZETA procedure in (Heimel et al. 2023), our procedure may be slightly less sensitive for small time windows because of the disruption of temporal correlation at the circular permutation wraparound point. However, it uses data only from within the time window of interest, so is less sensitive to unrelated modulation due to events occurring just outside the time window of interest; and it is much faster to compute. We performed this procedure for cue-locked (-200 ms to +400 ms), lift-locked (-200 ms to +400 ms), and first-contact-locked (-300 ms to 300 ms) data, for left and right trials separately.

RADICaL modeling

RADICaL models were fit using the same procedures developed in (Zhu et al. 2022) except we trained these models using the NeuroCAAS implementation (Abe et al. 2022). As in (Zhu et al. 2022), we used lift-locked data binned at 10 ms in a window from -100 to +800 ms around lift time with 100 ms padding. After models were fit, the padding was removed and RADICaL-inferred rates for each ROI were handled identically to sub-frame aligned smoothed and deconvolved data. Note that all results were qualitatively similar without RADICaL, but as expected decoding quality and correlations were generally somewhat lower.

Trial grouping

We observed considerable heterogeneity in the time from lift to spout contact (movement time) for both conditions for all mice. We reasoned that this could follow from single trial heterogeneity in either reach shape or accuracy. We therefore separated trials within each condition into two groups, determined by whether their movement time was smaller or greater

than the median movement time for that condition. This procedure yielded 4 groups of trials, “brief” and “long” for left and right conditions.

Peri-event time histograms

PETHs were computed for three different locking events: cue, lift and first contact. Neural data for all trials were binned at 10 ms and smoothed with a Gaussian (35 ms s.d.). Cue and lift-locked PETHs were locked in a window of -100 to 700 ms relative to the corresponding event. Contact-locked PETHs were locked in a window of -400 to 400 ms relative to first contact. Trials were then averaged within the groups described above.

Joint angle and velocity decoding

Joint angle or velocity kinematics were linearly interpolated from their original 6.66 ms to 10 ms and smoothed with a Gaussian (15 ms s.d.). We then screened for modulated neurons. Neurons deemed significant at a ZETA $p < 0.0083$ threshold for any behavioral events to either target were included. For decoding, neural and kinematic data were locked to -100 ms before and 400 ms lift onset. Deconvolved data were smoothed with a Gaussian (35 ms s.d.); RADICaL-inferred rates were not smoothed. We did not include a lag between neural activity and kinematics for simplicity; tests on selected sessions indicated that adding lags did not improve decoding. We applied PCA to the neural activity and reduced its dimensionality to be 90% of the number of included neurons. The decoder was trained and tested using cross-validated ridge regression. We partitioned the trials into 10 non-overlapping training (90%) and test (10%) set splits and fit the regularization parameter on the training set using a heuristic described in (Karabatsos 2018) with code developed in (Musall et al. 2019). We then applied the trained decoder to the test set and computed the fraction variance explained for each joint angle or velocity independently. We then repeated this same procedure for four additional 10-fold partitions for a total of 50 cross-validated folds. We report the variance explained across joints for all folds. To visualize reconstructions of the joint angles using the fit decoders, for each trial we “bagged” the decoder weights: we averaged across the 5 cross-validation folds where that trial was in the test set. This produced a denoised decoder that was used to predict the joint kinematics for that trial.

Target decoding analysis

We used logistic regression to classify individual time points as belonging to rightward or leftward targets from population activity. Neurons with significant modulation at a ZETA $p < 0.01$ threshold for any locking event and either target were included. Neural data from each trial were binned at 10 ms, locked to a window of -100 ms to 500 ms centered on cue onset, and smoothed with a Gaussian (35 ms s.d.). We partitioned the trials into five non-overlapping training (80%) and test (20%) set splits, stratifying left and right trials. We then trained a logistic regression classifier using the MATLAB *fitclinear* function on all post-cue time points across training set trials. We then projected individual trials onto the classifier dimension. We normalized each trial’s projection according to the 90th percentile value over all time points of the same trial type. We report the classifier performance on all time points across test set trials. Our procedure for computing the threshold crossing times for individual trials was similar to the one used in (Kaufman et al. 2015). We computed the threshold value by first taking the median

of all projections across trials at each time point, finding the maximum and minimum values of this trace, then computing their midpoint; this procedure was done separately for left and right trials. We found the threshold crossing time as the first time bin after which the projection stayed above the threshold for at least five consecutive bins (50 ms). If trials never crossed the threshold, or did not stay above threshold for more than five bins, they were discarded. We then interpolated between 10 ms bins to find the exact time that the projection crossed the threshold.

Time-generalized target decoding analysis

To assess the stability of the target-classifier dimension over time, we employed a similar logistic regression approach as above. Neural data from each trial were first interpolated as usual to 10 ms bins from -100 to 1000 ms relative to the cue, then smoothed with a Gaussian (35 ms s.d.). Time bins were then grouped into 11 non-overlapping 100 ms epochs. For each epoch, logistic regression was used to classify individual 10 ms time bins as belonging to left or right trials. A separate classifier was trained for each epoch, and thus 11 models were fit in total. This procedure was performed using 5-fold cross validation, with left and right trials stratified. The trained models for each epoch were used to predict the target identity on time points across all epochs for the held out 20% of trials from each fold. We reported the mean performance of the classifier over folds for each prediction epoch.

Reaction time decoding analysis

Deconvolved neural data were used to predict the lift reaction time (RT) on single trials. Our approach follows closely the procedure used in (Zhu et al. 2022) based on (Kaufman et al. 2016). A cross-validated logistic regression classifier was trained to discriminate pre-lift neural data (a bin -100 to 0 ms relative to lift onset) from post-lift neural data (a bin 0 to 100 ms relative to lift onset). Training was performed with *fitclinear* in Matlab, stratifying left and right trials. Neural data from the held-out trials was interpolated at 10 ms as usual, locked -200 to 600 ms relative to the lift, smoothed with a Gaussian (10 ms s.d.), then projected onto this dimension. The lift RT was calculated as the time that the projection crossed a threshold. To compute the threshold, we calculated the median across trials, then took the midpoint of the maximum and minimum. We summed the predicted time (which was effectively an offset from the true RT) with the ground truth lift RTs and correlated these with the ground truth lift RTs.

Abe T, **Kinsella I**, **Saxena S**, **Buchanan EK**, **Couto J**, **Briggs J**, **Kitt SL**, **Glassman R**, **Zhou J**, **Paninski L**, **Cunningham JP**. Neuroscience Cloud Analysis As a Service: An open-source platform for scalable, reproducible data analysis. *Neuron* 110: 2771-2789.e7, 2022.
Alonso I, **Scheer I**, **Palacio-Manzano M**, **Frézel-Jacob N**, **Philippides A**, **Prsa M**. Peripersonal encoding of forelimb proprioception in the mouse somatosensory cortex. *Nat Commun* 14: 1866, 2023.
Asanuma H. Recent developments in the study of the columnar arrangement of neurons within the motor cortex. *Physiol Rev* 55: 143–156, 1975.
Ashe J, **Georgopoulos AP**. Movement parameters and neural activity in motor cortex and area 5. *Cereb Cortex N Y N 1991* 4: 590–600, 1994.
Bollu T, **Whitehead SC**, **Prasad N**, **Walker J**, **Shyamkumar N**, **Subramaniam R**, **Kardon B**, **Cohen I**, **Goldberg JH**. Motor cortical inactivation impairs corrective submovements in mice performing a hold-still center-out reach task. *J Neurophysiol* 132: 829–848, 2024.
BRAIN Initiative Cell Census Network (BICCN), **BRAIN Initiative Cell Census Network (BICCN) Corresponding authors**, **Callaway EM**, **Dong H-W**, **Ecker JR**, **Hawrylycz MJ**, **Huang ZJ**, **Lein ES**, **Ngai J**, **Osten P**, **Ren B**, **Tolias AS**, **White O**, **Zeng H**, **Zhuang X**, **BICCN contributing principal investigators**, **Ascoli GA**, **Behrens MM**, **Chun J**, **Feng G**, **Gee JC**, **Ghosh SS**, **Halchenko YO**, **Hertzano R**, **Lim BK**, **Martone ME**, **Ng L**, **Pachter L**, **Ropelewski AJ**, **Tickle TL**, **Yang XW**, **Zhang K**, **Principal manuscript editors**, **Manuscript writing and figure generation**, **Bakken TE**, **Berens P**, **Daigle TL**, **Harris JA**, **Jorstad NL**, **Kalmbach BE**, **Kobak D**, **Li YE**, **Liu H**, **Matho KS**, **Mukamel EA**, **Naeemi M**, **Scala F**, **Tan P**, **Ting JT**, **Xie F**, **Zhang M**, **Zhang Z**, **Zhou J**, **Zingg B**, **Analysis coordination**, **Integrated data analysis**, **Armand E**, **Yao Z**, **scRNA-seq and snRNA-seq data generation and processing**, **Bertagnolli D**, **Casper T**, **Crichton K**, **Dee N**, **Diep D**, **Ding S-L**, **Dong W**, **Dougherty EL**, **Fong O**, **Goldman M**, **Goldy J**, **Hodge RD**, **Hu L**, **Keene CD**, **Krienen FM**, **Kroll M**, **Lake BB**, **Lathia K**, **Linnarsson S**, **Liu CS**, **Macosko EZ**, **McCarroll SA**, **McMillen D**, **Nadaf NM**, **Nguyen TN**, **Palmer CR**, **Pham T**, **Plongthongkum N**, **Reed NM**, **Regev A**, **Rimorin C**, **Romanow WJ**, **Savoia S**, **Siletti K**, **Smith K**, **Sulc J**, **Tasic B**, **Tieu M**, **Torkelson A**, **Tung H**, **van Velthoven CTJ**, **Vanderburg CR**, **Yanny AM**, **ATAC-seq data generation and processing**, **Fang R**, **Hou X**, **Lucero JD**, **Osteen JK**, **Pinto-Duarte A**, **Poirion O**, **Preissl S**, **Wang X**, **Methylcytosine data production and analysis**, **Aldridge AI**, **Bartlett A**, **Boggeman L**, **O'Connor C**, **Castanon RG**, **Chen H**, **Fitzpatrick C**, **Luo C**, **Nery JR**, **Nunn M**, **Rivkin AC**, **Tian W**, **Epi-retro-seq data generation and processing**, **Dominguez B**, **Ito-Cole T**, **Jacobs M**, **Jin X**, **Lee C-T**, **Lee K-F**, **Miyazaki PA**, **Pang Y**, **Rashid M**, **Smith JB**, **Vu M**, **Williams E**, **'Omics data analysis**, **Biancalani T**, **Booeshaghi AS**, **Crow M**, **Dudoit S**, **Fischer S**, **Gillis J**, **Hu Q**, **Kharchenko PV**, **Niu S-Y**, **Ntranos V**, **Purdom E**, **Risso D**, **de Bézieux HR**, **Somasundaram S**, **Street K**, **Svensson V**, **Vaishnav ED**, **Van den Berge K**, **Welch JD**, **Tracing and connectivity data generation**, **An X**, **Bateup HS**, **Bowman I**, **Chance RK**, **Foster NN**, **Galbavy W**, **Gong H**, **Gou L**, **Hatfield JT**, **Hintiryan H**, **Hirokawa KE**, **Kim G**, **Kramer DJ**, **Li A**, **Li X**, **Luo Q**, **Muñoz-Castañeda R**, **Stafford DA**, **Morphology data generation and reconstruction**, **Feng Z**, **Jia X**, **Jiang S**, **Jiang T**, **Kuang X**, **Larsen R**, **Lesnar P**, **Li Y**, **Li Y**, **Liu L**, **Peng H**, **Qu L**, **Ren M**, **Ruan Z**, **Shen E**, **Song Y**, **Wakeman W**, **Wang P**, **Wang Y**, **Wang Y**, **Yin L**, **Yuan J**, **Zhao S**, **Zhao X**, **OLST/STPT and other data generation**, **Narasimhan A**, **Palaniswamy R**, **Morphology, connectivity and imaging analysis**, **Banerjee S**, **Ding L**, **Huilgol D**, **Huo B**, **Kuo H-C**, **Laturnus S**, **Li X**, **Mitra PP**, **Mizrachi J**, **Wang Q**, **Xie P**, **Xiong F**, **Yu Y**, **Spatially resolved single-cell transcriptomics (MERFISH)**, **Eichhorn SW**, **Multimodal profiling (Patch-seq)**, **Berg J**, **Bernabucci M**, **Bernaerts Y**, **Cadwell CR**, **Castro JR**, **Dalley R**, **Hartmanis L**, **Horwitz GD**, **Jiang X**, **Ko AL**, **Miranda E**, **Mulherkar S**, **Nicovich PR**, **Owen SF**, **Sandberg R**, **Sorensen SA**, **Tan ZH**, **Transgenic tools**, **Allen S**, **Hockemeyer D**, **Lee AY**, **Veldman MB**, **NeMO archive and analytics**, **Adkins RS**, **Ament SA**, **Bravo HC**, **Carter R**, **Chatterjee A**, **Colantuoni C**,

Crabtree J, **Creasy H**, **Felix V**, **Giglio M**, **Herb BR**, **Kancherla J**, **Mahurkar A**, **McCracken C**, **Nickel L**, **Olley D**, **Orvis J**, **Schor M**, **Brain Image Library (BIL) archive**, **Hood G**, **DANDI archive**, **Dichter B**, **Grauer M**, **Helba B**, **Brain Cell Data Center (BCDC)**, **Bandrowski A**, **Barkas N**, **Carlin B**, **D'Orazi FD**, **Degatano K**, **Gillespie TH**, **Khajouei F**, **Konwar K**, **Thompson C**, **Project management**, **Kelly K**, **Mok S**, **Sunkin S**. A multimodal cell census and atlas of the mammalian primary motor cortex. *Nature* 598: 86–102, 2021.
Chowdhury RH, **Glaser JI**, **Miller LE**. Area 2 of primary somatosensory cortex encodes kinematics of the whole arm. *eLife* 9: e48198, 2020.
Cohen DA, **Prud'homme MJ**, **Kalaska JF**. Tactile activity in primate primary somatosensory cortex during active arm movements: correlation with receptive field properties. *J Neurophysiol* 71: 161–172, 1994.
Costanzo RM, **Gardner EP**. Multiple-joint neurons in somatosensory cortex of awake monkeys. *Brain Res* 214: 321–333, 1981.
Dacre J, **Colligan M**, **Clarke T**, **Ammer JJ**, **Schiemann J**, **Chamosa-Pino V**, **Claudi F**, **Harston JA**, **Eleftheriou C**, **Pakan JMP**, **Huang C-C**, **Hantman AW**, **Rochefort NL**, **Duguid I**. A cerebellar-thalamocortical pathway drives behavioral context-dependent movement initiation. *Neuron* 109: 2326-2338.e8, 2021.
Esposito MS, **Capelli P**, **Arber S**. Brainstem nucleus MdV mediates skilled forelimb motor tasks. *Nature* 508: 351–356, 2014.
Evarts EV. Motor Cortex Reflexes Associated with Learned Movement. *Science* 179: 501–503, 1973.
Evarts EV, **Fromm C**. Sensory responses in motor cortex neurons during precise motor control. *Neurosci Lett* 5: 267–272, 1977.
Feng Q, **He K**, **Wen H**, **Keskin C**, **Ye Y**. Rethinking the Data Annotation Process for Multi-view 3D Pose Estimation with Active Learning and Self-Training [Online]. arXiv2023.http://arxiv.org/abs/2112.13709 [27 Mar. 2023].
Fetz EE, **Finocchio DV**, **Baker MA**, **Soso MJ**. Sensory and motor responses of precentral cortex cells during comparable passive and active joint movements. *J Neurophysiol* 43: 1070–1089, 1980.
Friedrich J, **Zhou P**, **Paninski L**. Fast online deconvolution of calcium imaging data. *PLOS Comput Biol* 13: e1005423, 2017.
Fromm C, **Evarts EV**. Pyramidal tract neurons in somatosensory cortex: Central and peripheral inputs during voluntary movement. *Brain Res* 238: 186–191, 1982.
Fromm C, **Wise SP**, **Evarts EV**. Sensory response properties of pyramidal tract neurons in the precentral motor cortex and postcentral gyrus of the rhesus monkey. *Exp Brain Res* 54: 177–185, 1984.
Galiñanes GL, **Bonardi C**, **Huber D**. Directional Reaching for Water as a Cortex-Dependent Behavioral Framework for Mice. *Cell Rep* 22: 2767–2783, 2018.
Galinanes GL, **Huber D**. Continuous estimation of reaching space in superficial layers of the motor cortex. bioRxiv: 2023.12.01.569527, 2023.
Gardner EP, **Costanzo RM**. Properties of kinesthetic neurons in somatosensory cortex of awake monkeys. *Brain Res* 214: 301–319, 1981.
Georgopoulos AP, **Kalaska JF**, **Caminiti R**, **Massey JT**. On the relations between the direction of two-dimensional arm movements and cell discharge in primate motor cortex. *J Neurosci* 2: 1527–1537, 1982.
Georgopoulos AP, **Schwartz AB**, **Kettner RE**. Neuronal Population Coding of Movement Direction. *Science* 233: 1416–1419, 1986.
Goodman JM, **Tabot GA**, **Lee AS**, **Suresh AK**, **Rajan AT**, **Hatsopoulos NG**, **Bensmaia S**. Postural Representations of the Hand in the Primate Sensorimotor Cortex. *Neuron* 104: 1000-1009.e7, 2019.
Guo J-Z, **Graves AR**, **Guo WW**, **Zheng J**, **Lee A**, **Rodríguez-González J**, **Li N**, **Macklin JJ**,

Phillips JW, **Mensh BD**, **Branson K**, **Hantman AW**. Cortex commands the performance of skilled movement. *eLife* 4: e10774, 2015.
Guo J-Z, **Sauerbrei BA**, **Cohen JD**, **Mischiati M**, **Graves AR**, **Pisanello F**, **Branson KM**, **Hantman AW**. Disrupting cortico-cerebellar communication impairs dexterity. *eLife* 10: e65906, 2021.
Harrison TC, **Murphy TH**. Motor maps and the cortical control of movement. *Curr Opin Neurobiol* 24: 88–94, 2014.
Heimel JA, **Meijer GT**, **Montijn JS**. A new family of statistical tests for responses in point-event and time-series data for one- and two-sample comparisons. bioRxiv: 2023.10.30.564780, 2023.
Heindorf M, **Arber S**, **Keller GB**. Mouse Motor Cortex Coordinates the Behavioral Response to Unpredicted Sensory Feedback. *Neuron* 99: 1040-1054.e5, 2018.
Hwang EJ, **Dahlen JE**, **Hu YY**, **Aguilar K**, **Yu B**, **Mukundan M**, **Mitani A**, **Komiyama T**. Disengagement of motor cortex from movement control during long-term learning. *Sci Adv* 5: eaay0001, 2019.
Hwang EJ, **Dahlen JE**, **Mukundan M**, **Komiyama T**. Disengagement of Motor Cortex during Long-Term Learning Tracks the Performance Level of Learned Movements. *J Neurosci* 41: 7029–7047, 2021.
Inagaki HK, **Chen S**, **Ridder MC**, **Sah P**, **Li N**, **Yang Z**, **Hasanbegovic H**, **Gao Z**, **Gerfen CR**, **Svoboda K**. A midbrain-thalamus-cortex circuit reorganizes cortical dynamics to initiate movement. *Cell* 185: 1065-1081.e23, 2022.
Kakei S, **Hoffman DS**, **Strick PL**. Muscle and Movement Representations in the Primary Motor Cortex. *Science* 285: 2136–2139, 1999.
Kalaska JF, **Caminiti R**, **Georgopoulos AP**. Cortical mechanisms related to the direction of two-dimensional arm movements: relations in parietal area 5 and comparison with motor cortex. *Exp Brain Res* 51, 1983.
Karabatsos G. Marginal maximum likelihood estimation methods for the tuning parameters of ridge, power ridge, and generalized ridge regression. *Commun Stat - Simul Comput* 47: 1632–1651, 2018.
Kaufman MT, **Churchland MM**, **Ryu SI**, **Shenoy KV**. Vacillation, indecision and hesitation in moment-by-moment decoding of monkey motor cortex. *eLife* 4: e04677, 2015.
Kaufman MT, **Seely JS**, **Sussillo D**, **Ryu SI**, **Shenoy KV**, **Churchland MM**. The Largest Response Component in the Motor Cortex Reflects Movement Timing but Not Movement Type. *eNeuro* 3, 2016.
Kawai R, **Markman T**, **Poddar R**, **Ko R**, **Fantana AL**, **Dhawale AK**, **Kampff AR**, **Ölveczky BP**. Motor Cortex Is Required for Learning but Not for Executing a Motor Skill. *Neuron* 86: 800–812, 2015.
Lawrence DG, **Kuypers HGJM**. THE FUNCTIONAL ORGANIZATION OF THE MOTOR SYSTEM IN THE MONKEY: I. THE EFFECTS OF BILATERAL PYRAMIDAL LESIONS. *Brain* 91: 1–14, 1968.
Lemon R, **Hanby J**, **Porter R**. Relationship between the activity of precentral neurones during active and passive movements in conscious monkeys. *Proc R Soc Lond B Biol Sci* 194: 341–373, 1976.
Lemon RN, **Mantel GW**, **Muir RB**. Corticospinal facilitation of hand muscles during voluntary movement in the conscious monkey. *J Physiol* 381: 497–527, 1986.
Lucier GE, **Rüegg DC**, **Wiesendanger M**. Responses of neurones in motor cortex and in area 3A to controlled stretches of forelimb muscles in cebus monkeys. *J Physiol* 251: 833–853, 1975.
Makino H, **Hwang EJ**, **Hedrick NG**, **Komiyama T**. Circuit Mechanisms of Sensorimotor Learning. *Neuron* 92: 705–721, 2016.
Manley J, **Lu S**, **Barber K**, **Demas J**, **Kim H**, **Meyer D**, **Traub FM**, **Vaziri A**. Simultaneous, cortex-wide dynamics of up to 1 million neurons reveal unbounded scaling of dimensionality with neuron number. *Neuron* 112: 1694-1709.e5, 2024.

Marshall NJ, **Glaser JI**, **Trautmann EM**, **Amematsro EA**, **Perkins SM**, **Shadlen MN**, **Abbott LF**, **Cunningham JP**, **Churchland MM**. Flexible neural control of motor units. *Nat Neurosci* 25: 1492–1504, 2022.
Mathis A, **Mamidanna P**, **Cury KM**, **Abe T**, **Murthy VN**, **Mathis MW**, **Bethge M**. DeepLabCut: markerless pose estimation of user-defined body parts with deep learning. *Nat Neurosci* 21: 1281–1289, 2018.
Mathis MW, **Mathis A**, **Uchida N**. Somatosensory Cortex Plays an Essential Role in Forelimb Motor Adaptation in Mice. *Neuron* 93: 1493-1503.e6, 2017.
Miri A, **Warriner CL**, **Seely JS**, **Elsayed GF**, **Cunningham JP**, **Churchland MM**, **Jessell TM**. Behaviorally Selective Engagement of Short-Latency Effector Pathways by Motor Cortex. *Neuron* 95: 683-696.e11, 2017.
Mizes KGC, **Lindsey J**, **Escola GS**, **Ölveczky BP**. Motor cortex is required for flexible but not automatic motor sequences. bioRxiv: 2023.09.05.556348, 2023.
Mizes KGC, **Lindsey J**, **Escola GS**, **Ölveczky BP**. The role of motor cortex in motor sequence execution depends on demands for flexibility. *Nat Neurosci* 27: 2466–2475, 2024.
Montijn JS, **Seignette K**, **Howlett MH**, **Cazemier JL**, **Kamermans M**, **Levelt CN**, **Heimel JA**. A parameter-free statistical test for neuronal responsiveness. *eLife* 10: e71969, 2021.
Moran DW, **Schwartz AB**. Motor Cortical Representation of Speed and Direction During Reaching. *J Neurophysiol* 82: 2676–2692, 1999.
Morandell K, **Huber D**. The role of forelimb motor cortex areas in goal directed action in mice. *Sci Rep* 7: 15759, 2017.
Moreno-Lopez Y, **Bichara C**, **Delbecq G**, **Isope P**, **Cordero-Erausquin M**. The corticospinal tract primarily modulates sensory inputs in the mouse lumbar cord. *eLife* 10: e65304, 2021.
Moreno-López Y, **Olivares-Moreno R**, **Cordero-Erausquin M**, **Rojas-Piloni G**. Sensorimotor Integration by Corticospinal System. *Front Neuroanat* 10, 2016.
Morrow MM, **Miller LE**. Prediction of Muscle Activity by Populations of Sequentially Recorded Primary Motor Cortex Neurons. *J Neurophysiol* 89: 2279–2288, 2003.
Muñoz-Castañeda R, **Zingg B**, **Matho KS**, **Chen X**, **Wang Q**, **Foster NN**, **Li A**, **Narasimhan A**, **Hirokawa KE**, **Huo B**, **Bannerjee S**, **Korobkova L**, **Park CS**, **Park Y-G**, **Bienkowski MS**, **Chon U**, **Wheeler DW**, **Li X**, **Wang Y**, **Naeemi M**, **Xie P**, **Liu L**, **Kelly K**, **An X**, **Attili SM**, **Bowman I**, **Bludova A**, **Cetin A**, **Ding L**, **Drewes R**, **D'Orazi F**, **Elowsky C**, **Fischer S**, **Galbavy W**, **Gao L**, **Gillis J**, **Groblewski PA**, **Gou L**, **Hahn JD**, **Hatfield JT**, **Hintiryan H**, **Huang JJ**, **Kondo H**, **Kuang X**, **Lesnar P**, **Li X**, **Li Y**, **Lin M**, **Lo D**, **Mizrachi J**, **Mok S**, **Nicovich PR**, **Palaniswamy R**, **Palmer J**, **Qi X**, **Shen E**, **Sun Y-C**, **Tao HW**, **Wakemen W**, **Wang Y**, **Yao S**, **Yuan J**, **Zhan H**, **Zhu M**, **Ng L**, **Zhang LI**, **Lim BK**, **Hawrylycz M**, **Gong H**, **Gee JC**, **Kim Y**, **Chung K**, **Yang XW**, **Peng H**, **Luo Q**, **Mitra PP**, **Zador AM**, **Zeng H**, **Ascoli GA**, **Josh Huang Z**, **Osten P**, **Harris JA**, **Dong H-W**. Cellular anatomy of the mouse primary motor cortex. *Nature* 598: 159–166, 2021.
Musall S, **Kaufman MT**, **Juavinett AL**, **Gluf S**, **Churchland AK**. Single-trial neural dynamics are dominated by richly varied movements. *Nat Neurosci* 22: 1677–1686, 2019.
Naghizadeh M, **Mohajerani MH**, **Whishaw IQ**. Mouse Arm and hand movements in grooming are reaching movements: Evolution of reaching, handedness, and the thumbnail. *Behav Brain Res* 393: 112732, 2020.
Nelson RJ. Activity of monkey primary somatosensory cortical neurons changes prior to active movement. *Brain Res* 406: 402–407, 1987.
Nelson RJ. Interactions between motor commands and somatic perception in sensorimotor cortex. *Curr Opin Neurobiol* 6: 801–810, 1996.
Nicholas MA, **Yttri EA**. Motor cortex is responsible for motoric dynamics in striatum and the execution of both skilled and unskilled actions. *Neuron* 112: 3486-3501.e5, 2024.
O'Connor DH, **Krubitzer L**, **Bensmaia S**. Of mice and monkeys: Somatosensory processing in two prominent animal models. *Prog Neurobiol* 201: 102008, 2021.

Okorokova EV, **Goodman JM**, **Hatsopoulos NG**, **Bensmaia SJ**. Decoding hand kinematics from population responses in sensorimotor cortex during grasping. *J Neural Eng* 17: 046035, 2020.
Omlor W, **Wahl A-S**, **Sipilä P**, **Lütcke H**, **Laurenczy B**, **Chen I-W**, **Sumanovski LT**, **van 't Hoff M**, **Bethge P**, **Voigt FF**, **Schwab ME**, **Helmchen F**. Context-dependent limb movement encoding in neuronal populations of motor cortex. *Nat Commun* 10: 4812, 2019.
Omrani M, **Kaufman MT**, **Hatsopoulos NG**, **Cheney PD**. Perspectives on classical controversies about the motor cortex. *J Neurophysiol* 118: 1828–1848, 2017.
Park J, **Phillips JW**, **Guo J-Z**, **Martin KA**, **Hantman AW**, **Dudman JT**. Motor cortical output for skilled forelimb movement is selectively distributed across projection neuron classes. *Sci Adv* 8: eabj5167, 2022.
Pei Y-C, **Denchev PV**, **Hsiao SS**, **Craig JC**, **Bensmaia SJ**. Convergence of Submodality-Specific Input Onto Neurons in Primary Somatosensory Cortex. *J Neurophysiol* 102: 1843–1853, 2009.
Penfield W, **Boldrey E**. Somatic motor and sensory representation in the cerebral cortex of man as studied by electrical stimulation. *Brain* 60: 389–443, 1937.
Perich MG, **Conti S**, **Badi M**, **Bogaard A**, **Barra B**, **Rajan K**, **Bloch J**, **Courtine G**, **Micera S**, **Capogrosso M**, **Milekovic T**. Motor cortical dynamics are shaped by multiple distinct subspaces during naturalistic behavior. bioRxiv: 2020.07.30.228767, 2024.
Prsa M, **Morandell K**, **Cuenu G**, **Huber D**. Feature-selective encoding of substrate vibrations in the forelimb somatosensory cortex. *Nature* 567: 384–388, 2019.
Prud'homme MJ, **Kalaska JF**. Proprioceptive activity in primate primary somatosensory cortex during active arm reaching movements. *J Neurophysiol* 72: 2280–2301, 1994.
Ruder L, **Schina R**, **Kanodia H**, **Valencia-Garcia S**, **Pivetta C**, **Arber S**. A functional map for diverse forelimb actions within brainstem circuitry. *Nature* 590: 445–450, 2021.
Saleh M, **Takahashi K**, **Amit Y**, **Hatsopoulos NG**. Encoding of Coordinated Grasp Trajectories in Primary Motor Cortex. *J Neurosci* 30: 17079–17090, 2010.
Saleh M, **Takahashi K**, **Hatsopoulos NG**. Encoding of Coordinated Reach and Grasp Trajectories in Primary Motor Cortex. *J Neurosci* 32: 1220–1232, 2012.
Sauerbrei BA, **Guo J-Z**, **Cohen JD**, **Mischiati M**, **Guo W**, **Kabra M**, **Verma N**, **Mensh B**, **Branson K**, **Hantman AW**. Cortical pattern generation during dexterous movement is input-driven. *Nature* 577: 386–391, 2020.
Seki K, **Perlmutter SI**, **Fetz EE**. Sensory input to primate spinal cord is presynaptically inhibited during voluntary movement. *Nat Neurosci* 6: 1309–1316, 2003.
Steinmetz NA, **Aydin C**, **Lebedeva A**, **Okun M**, **Pachitariu M**, **Bauza M**, **Beau M**, **Bhagat J**, **Böhm C**, **Broux M**, **Chen S**, **Colonell J**, **Gardner RJ**, **Karsh B**, **Kloosterman F**, **Kostadinov D**, **Mora-Lopez C**, **O'Callaghan J**, **Park J**, **Putzeys J**, **Sauerbrei B**, **van Daal RJJ**, **Vollan AZ**, **Wang S**, **Welkenhuysen M**, **Ye Z**, **Dudman JT**, **Dutta B**, **Hantman AW**, **Harris KD**, **Lee AK**, **Moser EI**, **O'Keefe J**, **Renart A**, **Svoboda K**, **Häusser M**, **Haesler S**, **Carandini M**, **Harris TD**. Neuropixels 2.0: A miniaturized high-density probe for stable, long-term brain recordings. *Science* 372: eabf4588, 2021.
Steinmetz NA, **Zatka-Haas P**, **Carandini M**, **Harris KD**. Distributed coding of choice, action, and engagement across the mouse brain. *Nature* 576: 266–273, 2019.
Stringer C, **Pachitariu M**. Computational processing of neural recordings from calcium imaging data. *Curr Opin Neurobiol* 55: 22–31, 2019.
Stringer C, **Pachitariu M**, **Steinmetz N**, **Reddy CB**, **Carandini M**, **Harris KD**. Spontaneous behaviors drive multidimensional, brainwide activity. *Science* 364: eaav7893, 2019.
Tanji J, **Wise SP**. Submodality distribution in sensorimotor cortex of the unanesthetized monkey. *J Neurophysiol* 45: 467–481, 1981.
Tennant KA, **Adkins DL**, **Donlan NA**, **Asay AL**, **Thomas N**, **Kleim JA**, **Jones TA**. The Organization of the Forelimb Representation of the C57BL/6 Mouse Motor Cortex as Defined by

Intracortical Microstimulation and Cytoarchitecture. *Cereb Cortex* 21: 865–876, 2011.
Ueno M, **Nakamura Y**, **Li J**, **Gu Z**, **Niehaus J**, **Maezawa M**, **Crone SA**, **Goulding M**, **Baccei ML**, **Yoshida Y**. Corticospinal Circuits from the Sensory and Motor Cortices Differentially Regulate Skilled Movements through Distinct Spinal Interneurons. *Cell Rep* 23: 1286-1300.e7, 2018.
Umeda T, **Isa T**, **Nishimura Y**. The somatosensory cortex receives information about motor output. *Sci Adv* 5: eaaw5388, 2019.
Vargas-Irwin CE, **Shakhnarovich G**, **Yadollahpour P**, **Mislow JMK**, **Black MJ**, **Donoghue JP**. Decoding Complete Reach and Grasp Actions from Local Primary Motor Cortex Populations. *J Neurosci* 30: 9659–9669, 2010.
Wang W, **Chan SS**, **Heldman DA**, **Moran DW**. Motor Cortical Representation of Position and Velocity During Reaching. *J Neurophysiol* 97: 4258–4270, 2007.
Warriner CL, **Fageiry S**, **Saxena S**, **Costa RM**, **Miri A**. Motor cortical influence relies on task-specific activity covariation. *Cell Rep* 40: 111427, 2022.
Warriner CL, **Fageiry SK**, **Carmona LM**, **Miri A**. Towards Cell and Subtype Resolved Functional Organization: Mouse as a Model for the Cortical Control of Movement. *Neuroscience* 450: 151–160, 2020.
Weber DJ, **London BM**, **Hokanson JA**, **Ayers CA**, **Gaunt RA**, **Torres RR**, **Zaaimi B**, **Miller LE**. Limb-state information encoded by peripheral and central somatosensory neurons: implications for an afferent interface. *IEEE Trans Neural Syst Rehabil Eng Publ IEEE Eng Med Biol Soc* 19: 501–513, 2011.
Wei Z, **Lin B-J**, **Chen T-W**, **Daie K**, **Svoboda K**, **Druckmann S**. A comparison of neuronal population dynamics measured with calcium imaging and electrophysiology. *PLOS Comput Biol* 16: e1008198, 2020.
Whishaw IQ. An endpoint, descriptive, and kinematic comparison of skilled reaching in mice (Mus musculus) with rats (Rattus norvegicus). *Behav Brain Res* 78: 101–111, 1996.
Whishaw IQ, **Pellis SM**. The structure of skilled forelimb reaching in the rat: A proximally driven movement with a single distal rotatory component. *Behav Brain Res* 41: 49–59, 1990.
Whishaw IQ, **Pellis SM**, **Gorny B**, **Kolb B**, **Tetzlaff W**. Proximal and distal impairments in rat forelimb use in reaching follow unilateral pyramidal tract lesions. *Behav Brain Res* 56: 59–76, 1993.
Whishaw IQ, **Travis SG**, **Koppe SW**, **Sacrey L-A**, **Gholamrezaei G**, **Gorny B**. Hand shaping in the rat: conserved release and collection vs. flexible manipulation in overground walking, ladder rung walking, cylinder exploration, and skilled reaching. *Behav Brain Res* 206: 21–31, 2010.
Winnubst J, **Bas E**, **Ferreira TA**, **Wu Z**, **Economo MN**, **Edson P**, **Arthur BJ**, **Bruns C**, **Rokicki K**, **Schauder D**, **Olbris DJ**, **Murphy SD**, **Ackerman DG**, **Arshadi C**, **Baldwin P**, **Blake R**, **Elsayed A**, **Hasan M**, **Ramirez D**, **Dos Santos B**, **Weldon M**, **Zafar A**, **Dudman JT**, **Gerfen CR**, **Hantman AW**, **Korff W**, **Sternson SM**, **Spruston N**, **Svoboda K**, **Chandrashekar J**. Reconstruction of 1,000 Projection Neurons Reveals New Cell Types and Organization of Long-Range Connectivity in the Mouse Brain. *Cell* 179: 268-281.e13, 2019.
Wolff SBE, **Ko R**, **Ölveczky BP**. Distinct roles for motor cortical and thalamic inputs to striatum during motor skill learning and execution. *Sci Adv* 8: eabk0231, 2022.
Wong YC, **Kwan HC**, **MacKay WA**, **Murphy JT**. Spatial organization of precentral cortex in awake primates. I. Somatosensory inputs. *J Neurophysiol* 41: 1107–1119, 1978.
Yamawaki N, **Raineri Tapies MG**, **Stults A**, **Smith GA**, **Shepherd GM**. Circuit organization of the excitatory sensorimotor loop through hand/forelimb S1 and M1. *eLife* 10: e66836, 2021.
Yang W, **Kanodia H**, **Arber S**. Structural and functional map for forelimb movement phases between cortex and medulla. *Cell* 186: 162-177.e18, 2023.
Yu BM, **Cunningham JP**, **Santhanam G**, **Ryu SI**, **Shenoy KV**, **Sahani M**. Gaussian-Process Factor Analysis for Low-Dimensional Single-Trial Analysis of Neural Population Activity. *J*

Neurophysiol 102: 614–635, 2009.
Yu C-H, **Stirman JN**, **Yu Y**, **Hira R**, **Smith SL**. Diesel2p mesoscope with dual independent scan engines for flexible capture of dynamics in distributed neural circuitry. *Nat Commun* 12: 6639, 2021.
Zhu F, **Grier HA**, **Tandon R**, **Cai C**, **Agarwal A**, **Giovannucci A**, **Kaufman MT**, **Pandarinath C**. A deep learning framework for inference of single-trial neural population dynamics from calcium imaging with subframe temporal resolution. *Nat Neurosci* 25: 1724–1734, 2022.
Zingg B, **Hintiryan H**, **Gou L**, **Song MY**, **Bay M**, **Bienkowski MS**, **Foster NN**, **Yamashita S**, **Bowman I**, **Toga AW**, **Dong H-W**. Neural networks of the mouse neocortex. *Cell* 156: 1096–1111, 2014.

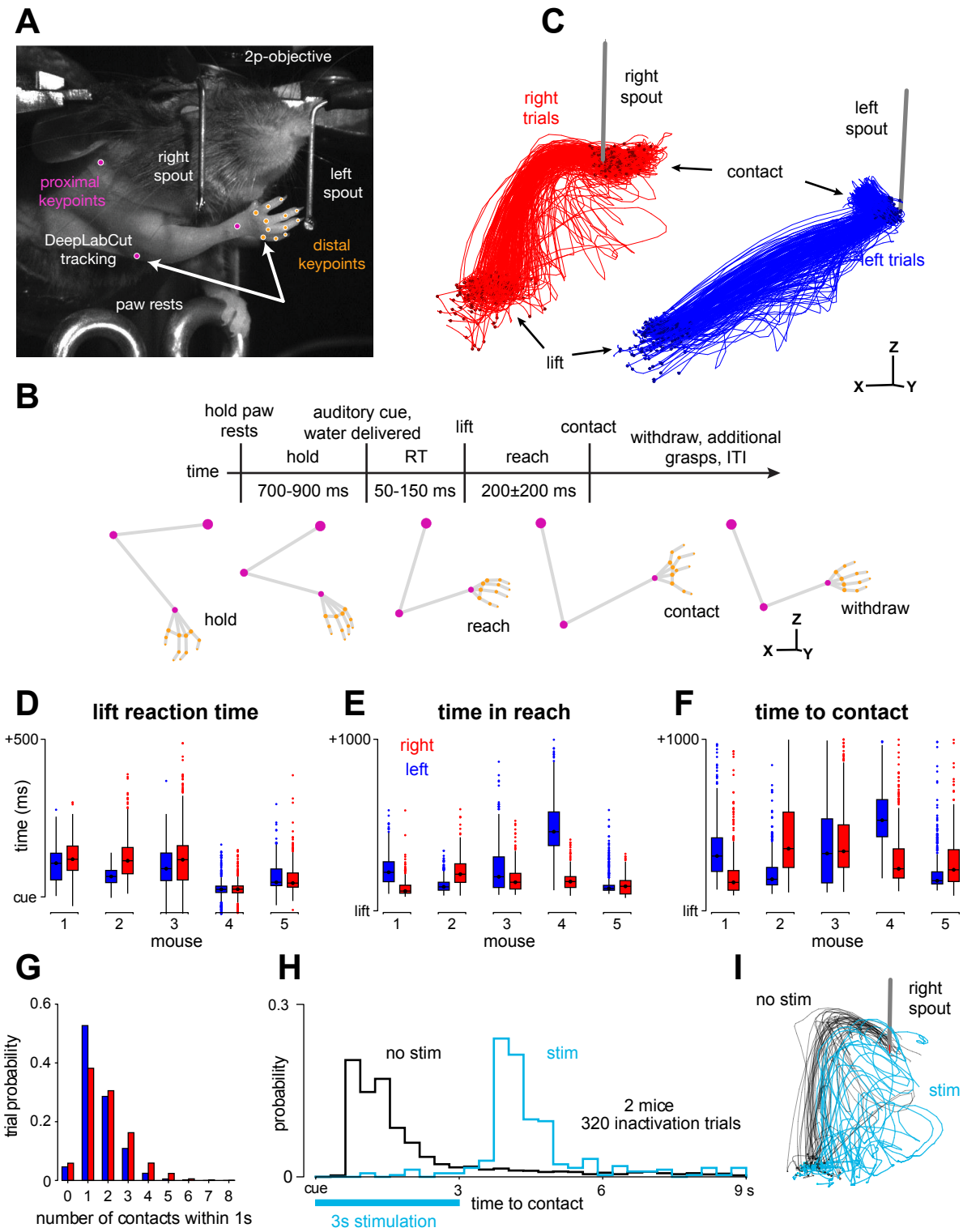

Figure 1: Mice make complex reaching and grasping movements to retrieve water rewards during head-fixation (A) Task setup: a head-fixed animal mid-reach with representative markerless tracking. (B) Task timeline, with representative 3D triangulated forelimb "skeletons". (C) Distal digit centroid trajectories from 100 ms before lift to 100 ms after contact, left and right trials offset for visualization. One example session. (D) Lift reaction time distributions, left and right trials depicted separately. (E) Time from lift to paw centroid arriving within 5 mm of the spout target tip. (F) Time between lift and spout contact. Box plots in D-F show the quartiles (box and central line), whiskers extend 1.5 times the interquartile range past the quartile boundary, and more distant points (outliers) are plotted individually. (G) Number of contact events within 1 second of the water cue per trial. Data were pooled across sessions for D-G. (H) Time between cue and spout contact during optogenetic experiments. (I) Representative digit centroid trajectories for a subset of right trials during optogenetic experiments, from -100 ms before lift to 1000 ms after lift. Data from one example session.

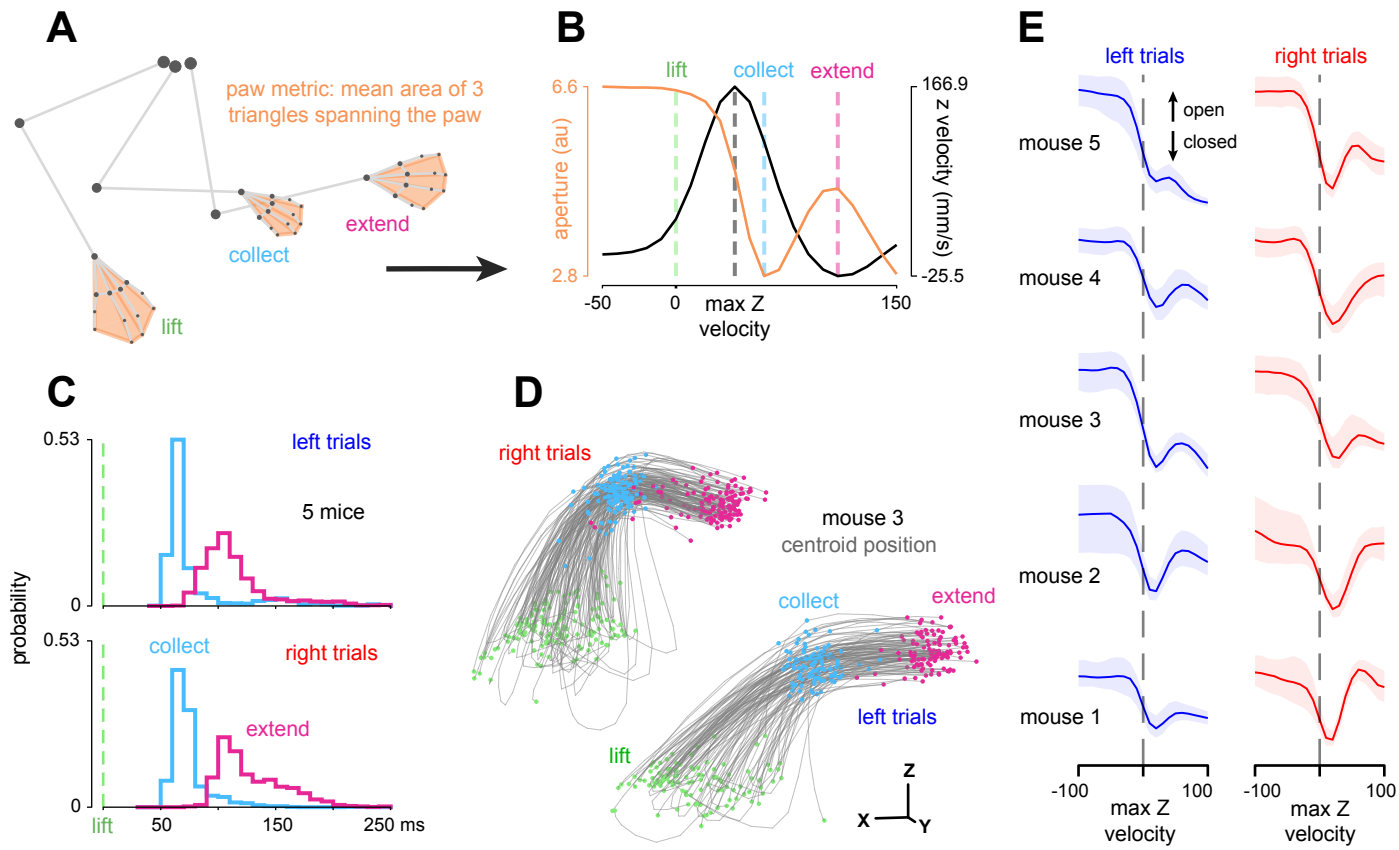

Figure 2: Paw aperture reveals stereotyped kinematics across idiosyncratic single trial reach-to-grasp movements (A) Paw aperture was computed from the paw markers using a simple geometric measure. (B) Aperture time series overlaid on the Z velocity of the paw centroid. The collect and extend events are defined by the aperture minimum and its subsequent local maximum. Representative trial. (C) Histograms of collect and extend event times for all trials, left and right trials separated. (D) Lift, collect and extend event times depicted on digit centroid trajectories for one example mouse. (E) Median over trials of aperture time series aligned to the moment of maximum centroid Z velocity.

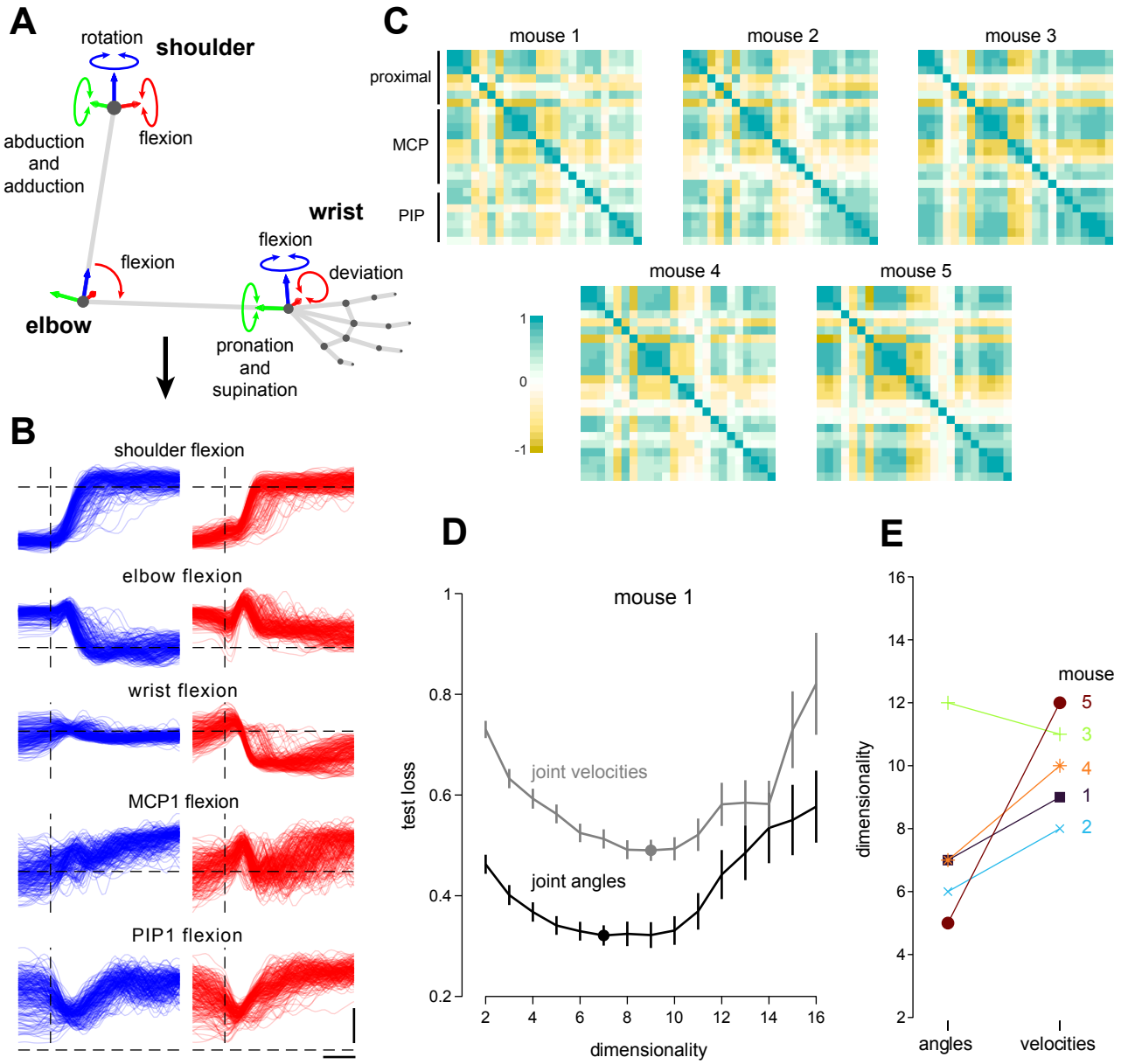

Figure 3: Mouse reaching and grasping movements involve coordination across proximal and distal joints (A) Schematic of Euler angle inverse kinematics procedure, depicting 7 joint angles over the proximal joints; 17 distal angles not shown. (B) Time series of 5 representative joints, shown from -100 ms to +400 ms around lift onset (vertical dashed line). Left (blue) and right (red) trials shown separately. Horizontal scale bar is 100 ms. Vertical scale bar is 30 degrees. Dashed horizontal lines are 0 degrees. (C) Correlation matrices of joint angles over all recorded time points. Rows are ordered descending from proximal (shoulder) to distal (metacarpal phalanges, MCP, proximal interphalanges, PIP). (D) Example loss curve of the cross-validated principal component analysis performed on joint angle and joint velocity time series. (E) Estimated dimensionalities of joint angle and velocity kinematics across mice.

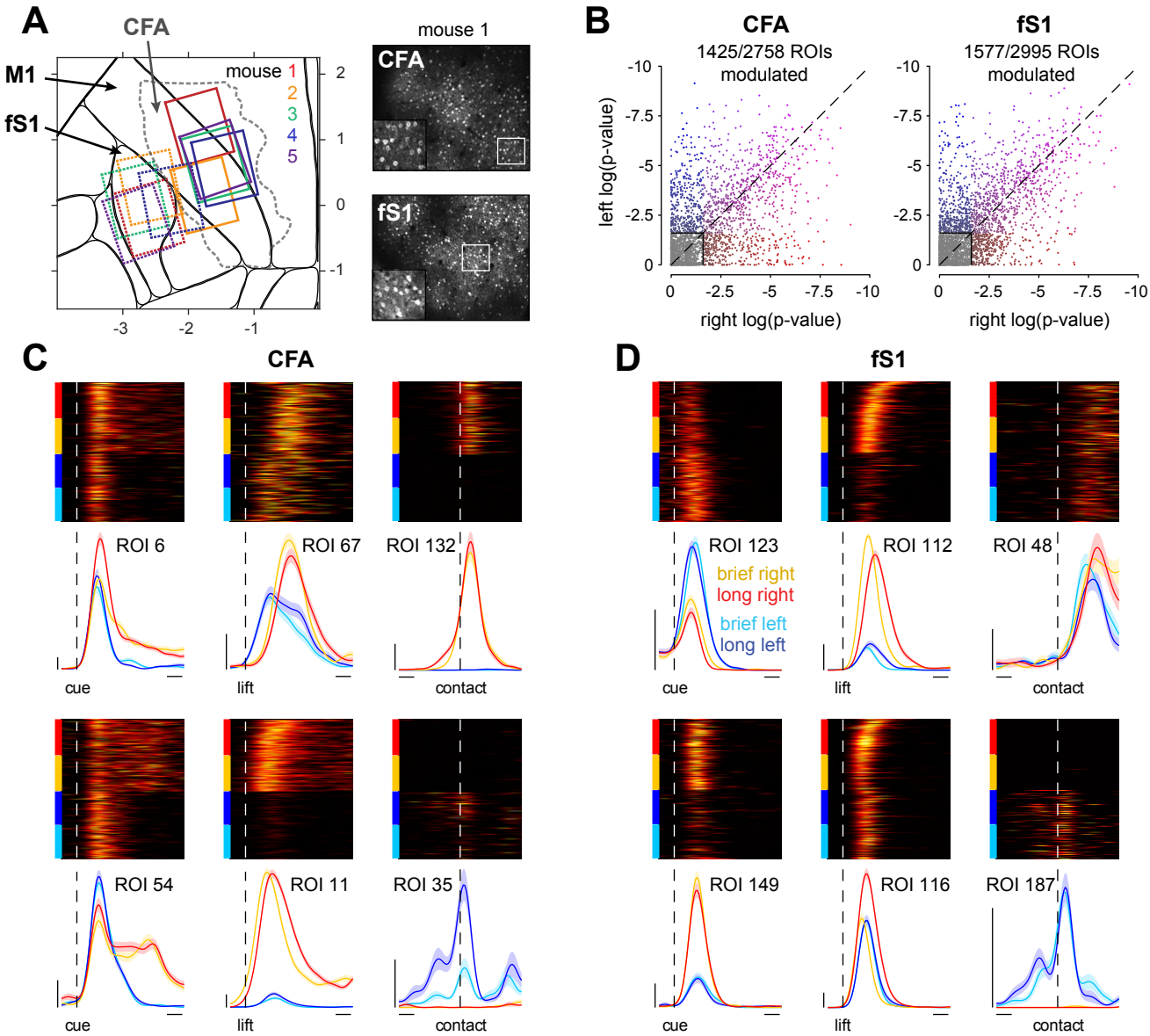

Figure 4: CFA and fS1 cells are heterogeneously tuned to specific movement features (A) 2-photon imaging fields of view for all mice aligned to the Allen Atlas common coordinate framework (CCF). fS1 corresponds to SSp-ul and M1 to MOp in the CCF. The dashed gray line indicates the outline of the forelimb primary motor cortex (MOp-ul, referred to here as CFA) as described in Muñoz-Castañeda et al 2021. See Figure 4S1 and Methods for field of view alignment details. Right, example max-projection images for CFA and fS1 for mouse 1 with magnified insets. M1 and fS1 correspond to MOp and SSp-fl in the Allen CCF nomenclature. (B) Modulation metric (see Methods) of cue-locked data for individual cells in CFA and fS1. Values displayed are the logarithm of the computed p-value, where each point represents a cell. All cells with p-values < 0.025 are shown colored: left-only modulated cells are blue, right-only modulated cells are red, and cells modulated to both conditions are purple. (C) Peri-event histograms and rasters of single trial activity from individual cells in CFA. Each column displays two cells locked to each trial event: cue, lift and first-spout-contact. Trials grouped within each condition by time-in-reach. Vertical scale bar: 10 events per second (arbitrary units). Horizontal scale bar: 100 ms. (D) As in C but for fS1.

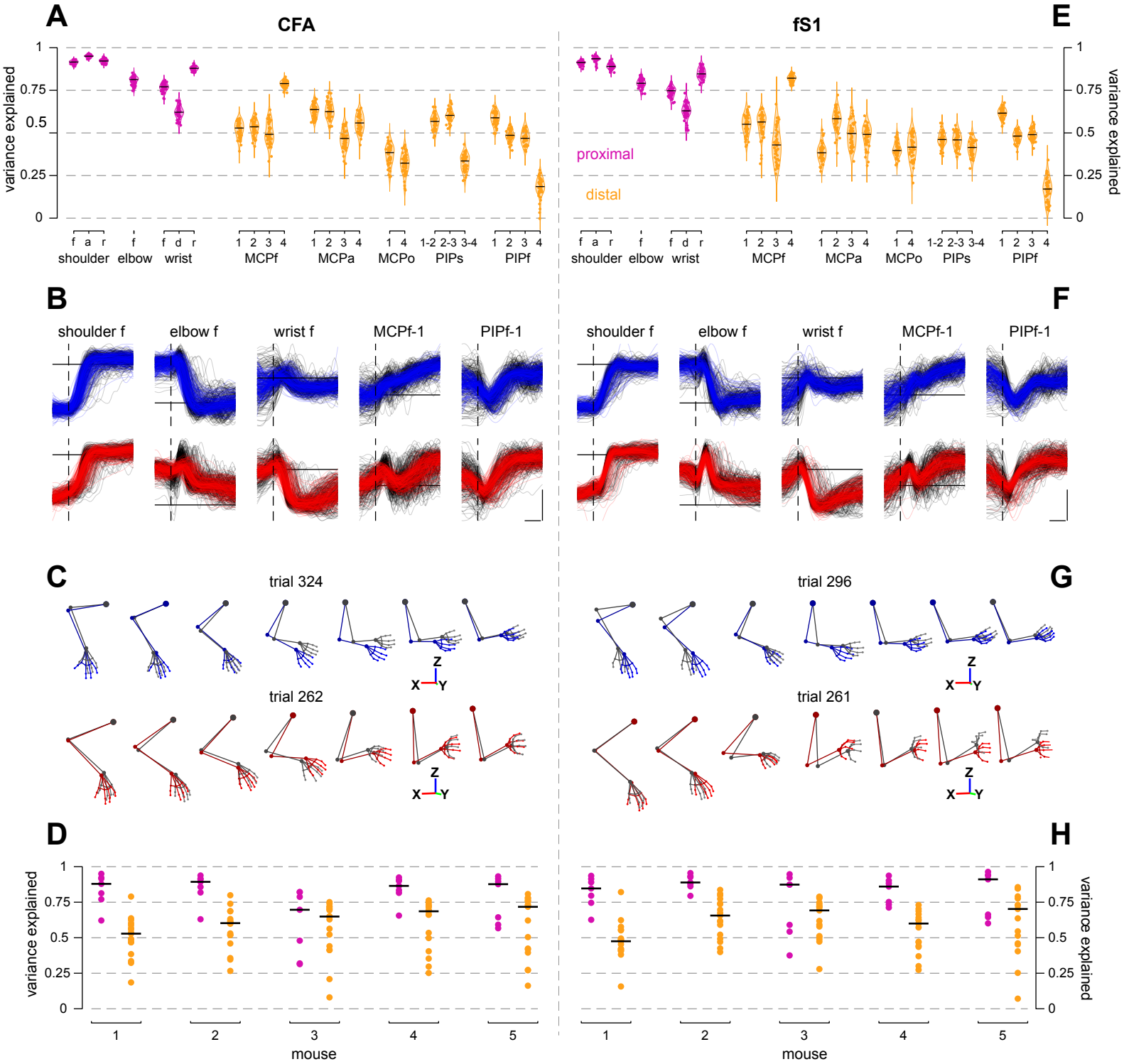

Figure 5: Kinematic details of proximal and distal joints during reaching and grasping can be decoded from CFA and fS1 population activity (A) Performance of decoding models predicting joint angle kinematics from RADICaL-inferred CFA rates. Violins depict the distribution of variance explained over cross-validation folds for each individual joint angle. (f: flexion, a: abduction/adduction, r: rotation, d: deviation, o: opposition, s: splay, MCP: metacarpal-phalanges, PIP: proximal-interphalanges; digits indicated by number). (B) Reconstructed joint angle time series for 5 representative joint angles. Black traces are original and colored are reconstructed; left trials are blue and right trials are red. Vertical dashed line indicates lift time, horizontal line indicates 0 degrees. Vertical scale bar is 30 degrees, horizontal scale bar is 100 ms. (C) Forelimb skeletal postures reconstructed from decoded joint angles for representative left and right trials (trials having median variance explained). 7 representative time points from lift time to grab time are shown. Gray postures are original data, colored postures are reconstructed as in B. Decoded joint angles in each time step were applied to the neutralized posture of the original data, preserving the original lengths of inter-marker links. (D). Performance of decoding models for all 5 mice. Each point is the median of the distribution of variance explained over cross validation folds, with proximal (magenta) and distal (goldenrod) angles considered separately. The black lines indicate the median variance explained over all proximal or distal joints for an individual mouse. (E-H) As in A-D but for fS1 data.

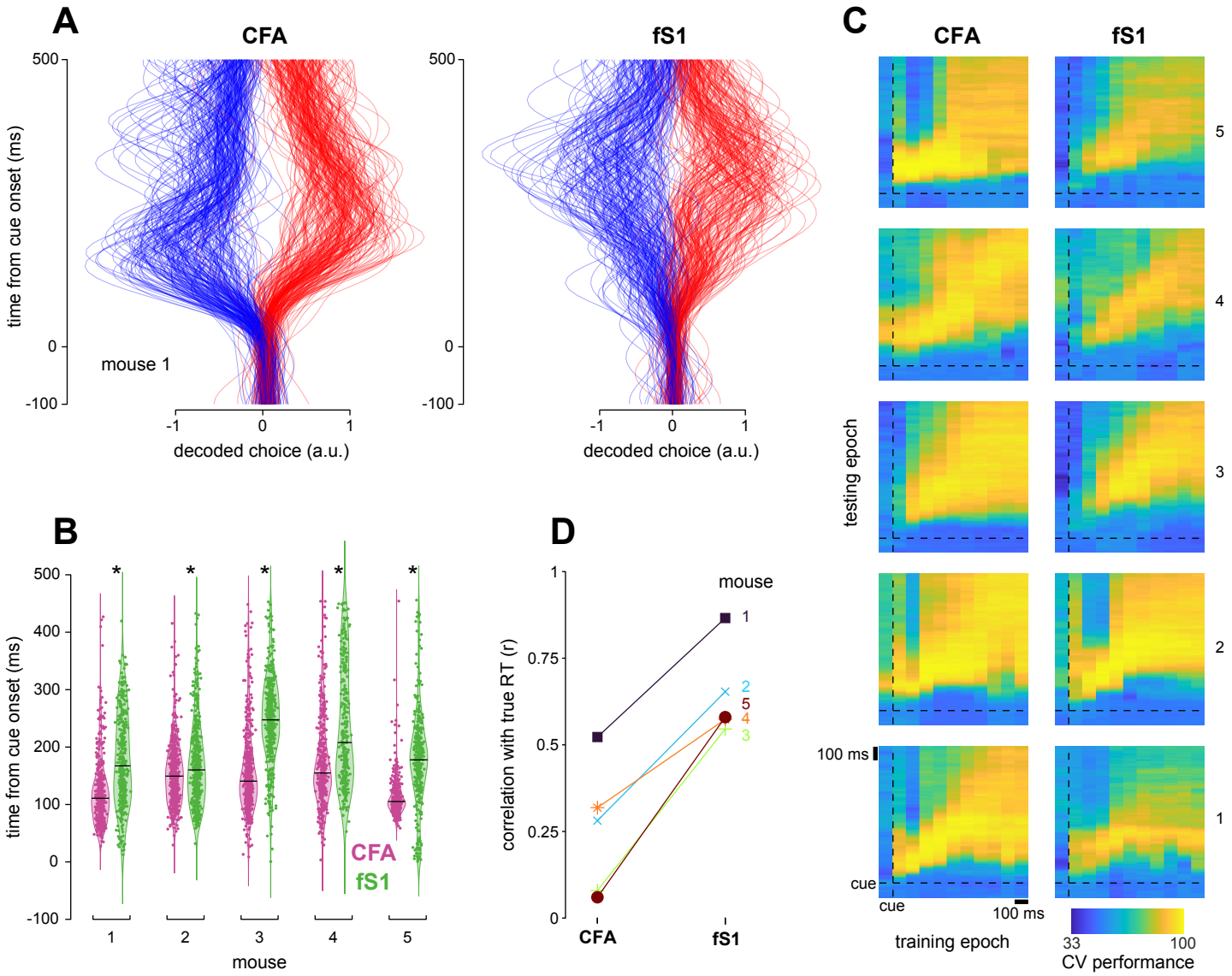

Figure 6: CFA reflects target-specific information earlier and more persistently than fS1 (A) Projections of population activity from held-out single trials onto the target decoding dimension for CFA and fS1. Right trials are red and left trials are blue. Traces were normalized by the 90th percentile value across trials for left and right trials separately. (B) Distribution of threshold crossing times for projections shown in A. Black lines indicate medians. Star indicates significantly different medians at $p < 0.05$, Wilcoxon ranksum. (C) Performance of time-generalized target decoding analysis. Each heat map depicts the performance over all model training windows (columns) and test time points (rows). Time in trial runs vertically as in A. Both the training and testing epochs were -100 (leftmost column training, bottommost row test) to +1000 ms (rightmost column training, top row test) relative to cue. Training epochs were 100 ms non-overlapping windows and testing epochs were 10 ms bins.

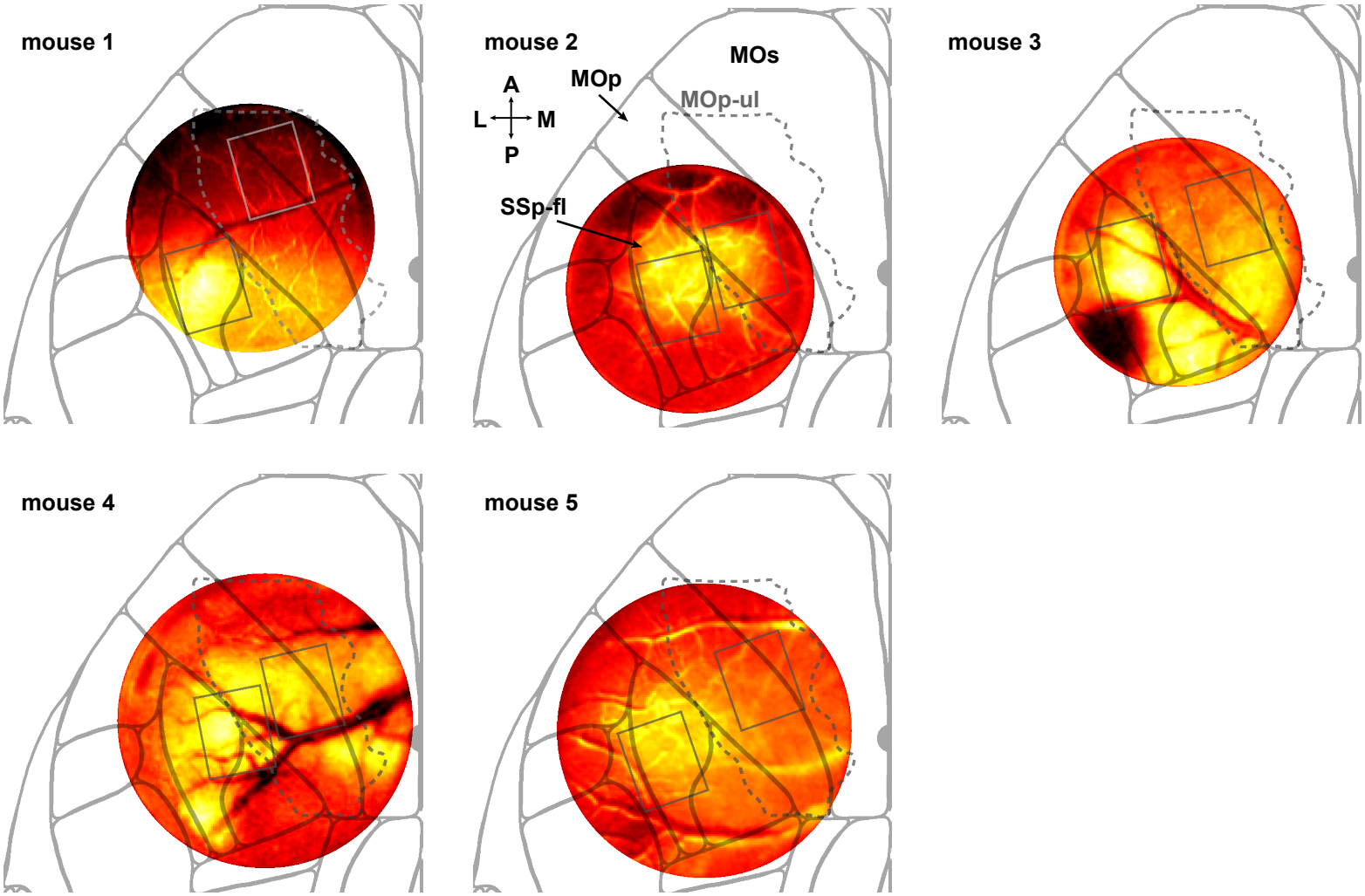

Figure 4S1: Vibration mapping for each individual mouse. Each image shows the widefield calcium response +250 ms after a vibrational stimulus applied to the contralateral paw. Each image was aligned with the underlying Allen CCF by placing the broad fS1 (SSp-fl in the Allen nomenclature) shaped activity profile within the corresponding region. Placement was then verified against veridical injection coordinates obtained during surgery (not shown). The dashed line in each map indicates the outline of the forelimb primary motor cortex (MOp-ul) as described in Muñoz-Castañeda et al 2021. Each grey box indicates the placement of the imaging fields of view in CFA and fS1 for each animal. Note that the window for mouse 1 was tilted anterior-posterior during widefield imaging, reducing the measured response in the anterior half of the window. This was accounted for in estimating atlas alignment.

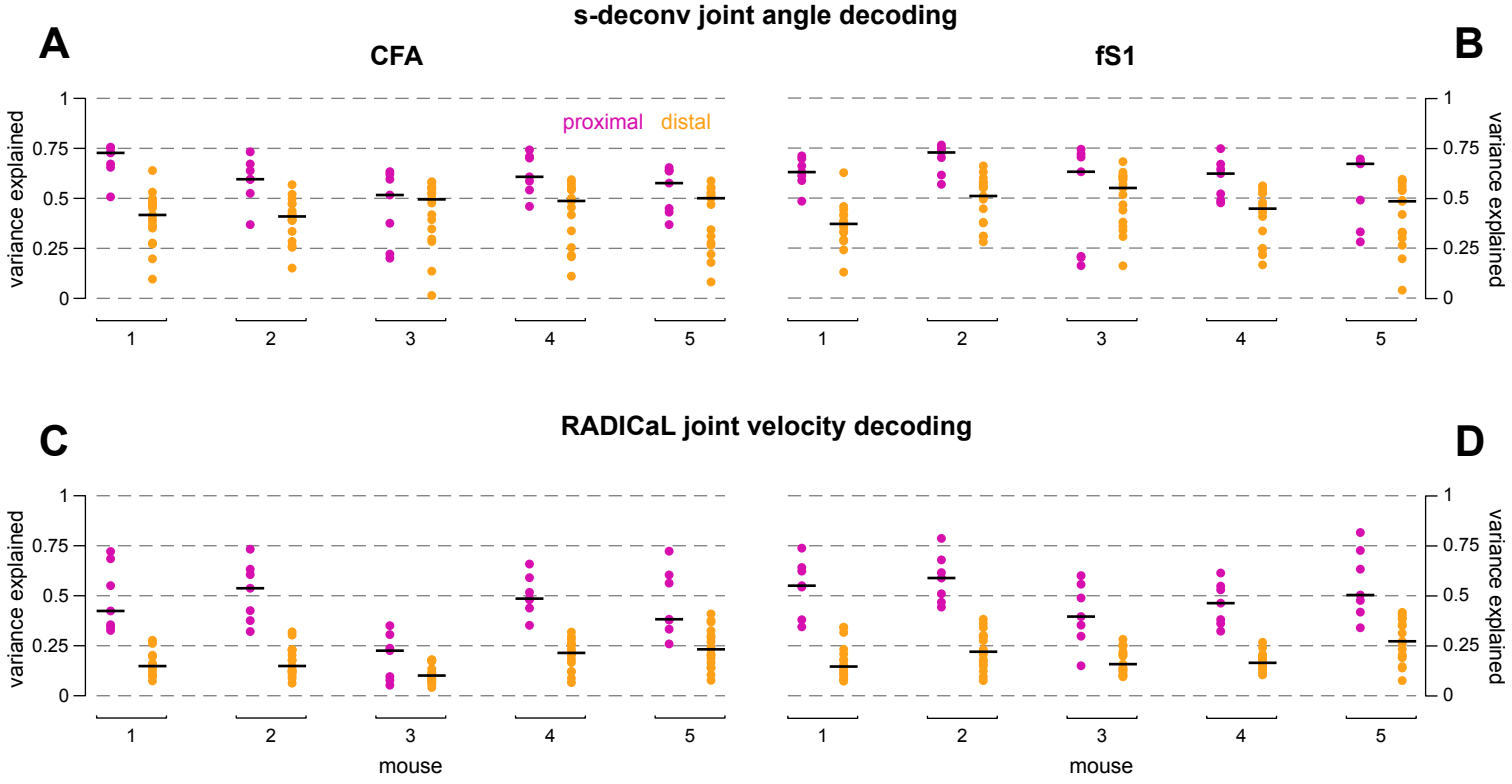

Figure 5S1: (A) Joint angle decoding as in Figure 5, but from CFA deconvolved calcium transients smoothed with a 35 ms Gaussian kernel. Data is presented as in Figure 5D and 5H. (B) as in A but for fS1. (C) Joint velocity decoding using RADICaL rates from CFA. (D) Same as C but for fS1.

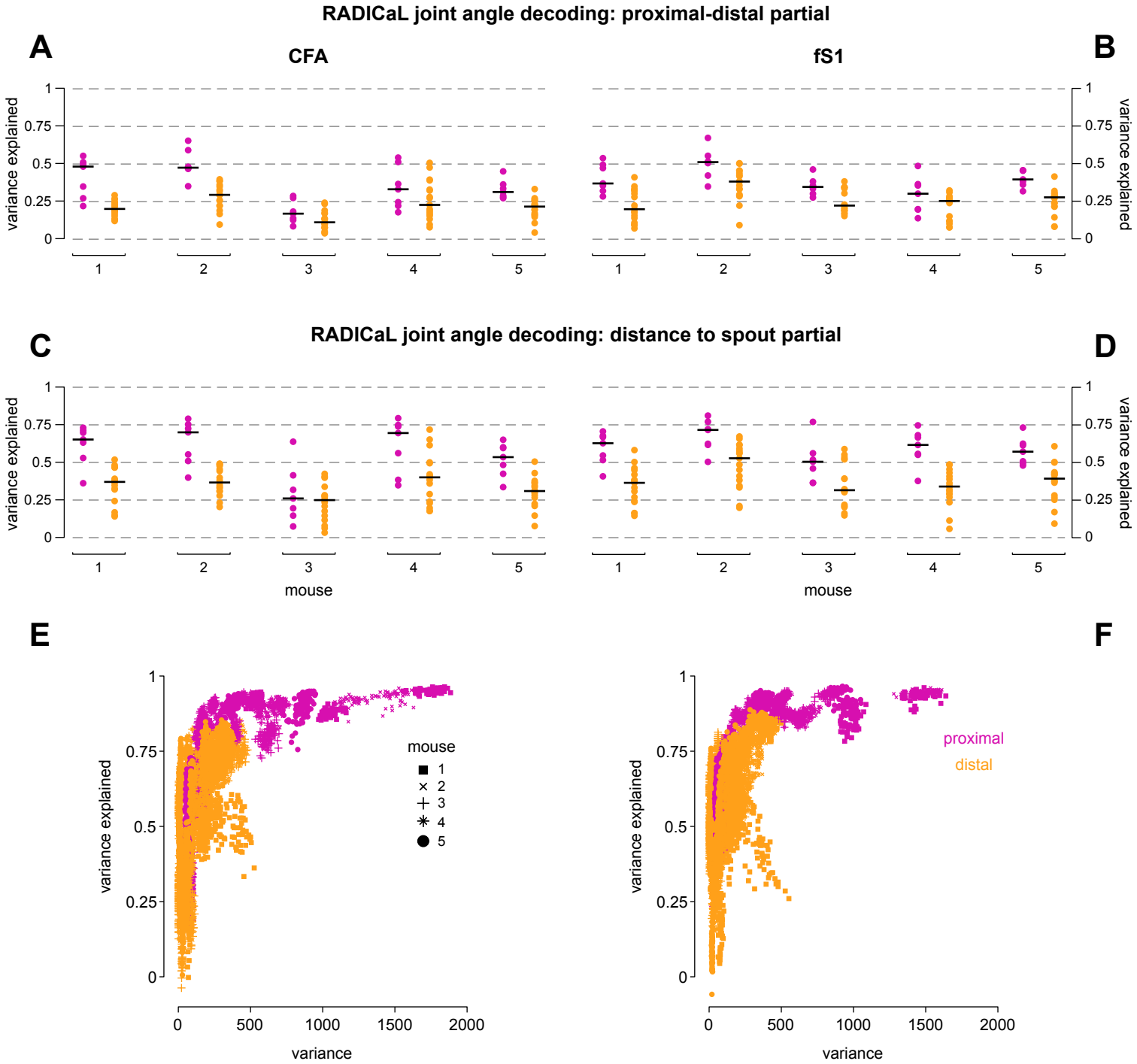

Figure 5S2: (A) Joint angle decoding as in Figure 5 but with proximal joint angle time series regressed off of distal joints and distal joint angle time series regressed off of proximal joints. Decoding performed with RADICaL rates. Data is presented as in Figure 5D and 5H. (B) as in A but for fS1. (C) Joint angle decoding as in Figure 5 but with the distance to the spout of the paw centroid regressed off of all joint angles. (D) Same as C but for S1-fl. (E) Variance of joint angles and their variance explained when decoded using CFA RADICaL rates as in Figure 5. Each point has coordinates of the true kinematic variance and the variance explained for a single joint on a single cross-validation fold. (F) Same as E but for fS1.